Clouds and precipitation in the initial phase of marine cold air outbreaks as observed by airborne remote sensing

Imke Schirmacher[1], Sabrina Schnitt[1], Marcus Klingebiel[2], Nina Maherndl[2], Benjamin Kirbus[2], André Ehrlich[2], Mario Mech[1], and Susanne Crewell[1]

[1]Institute for Geophysics and Meteorology, University of Cologne, Cologne, Germany
[2]Institute for Meteorology, Leipzig University, Leipzig, Germany

Correspondence: Imke Schirmacher (imke.schirmacher@uni-koeln.de)

Abstract. Marine cold air outbreaks (MCAOs) strongly affect the Arctic water cycle and, thus, climate through large-scale air mass transformations. The description of air mass transformations is still challenging, partly because previous observations do not resolve fine scales, particularly for the initial development of ~~a~~ an MCAO, and lack information about the thermodynamical evolution starting over sea ice and continuing over open ocean and associated cloud microphysical properties. Therefore, we focus on the crucial initial development within the first 200 km over open water ~~of two MCAO events with different strengths observed~~ for two case studies in April 2022 during the HALO-(AC)³ campaign. ~~Based on unique sampling of high-resolution airborne remote sensing and in-situ measurements, the development of the boundary layer, formation of clouds, onset of precipitation, and riming are studied. For this purpose, we establish a novel approach, solely based on radar reflectivity measurements, to detect roll circulation that forms cloud streets.~~

~~The two MCAO events observed in April 2022~~ The two events, just three days apart, belong to a particularly long-lasting MCAO and occurred under relatively similar thermodynamic conditions. However, for the first event, colder airmasses from the central Arctic led to ~~a marine cold air outbreak index twice that~~ an MCAO index twice as high as for the second event~~. Thus, the~~, though both events were stronger than the climatological 75th percentile for that period.

The evolution and structure were assessed by flight legs crossing the Fram Strait multiple times, sampling perpendicular to the cloud streets. Airborne remote sensing and in-situ measurements were used to build statistical descriptions of the boundary layer, dynamics, clouds, and precipitation. For this purpose, we established a novel approach based solely on radar reflectivity measurements to detect roll circulation that forms cloud streets. The two cases exhibit different properties of clouds, riming, and roll circulations though the width of the roll circulation is similar. For the stronger ~~MCAO~~event, cloud tops are higher, more liquid-topped clouds exist, the liquid ~~layer at cloud top is wider, and the liquid~~ water path, mean radar reflectivity, precipitation rate, and ~~occurrence are increased. These parameters~~ precipitation occurrence have increased, and riming is active. The variability of rime mass has the same horizontal scale as the roll circulation, implying the importance of roll circulation on cloud microphysics and precipitation.

Boundary layer and cloud properties evolve with distance over open water, as seen by, e.g., ~~boundary layer deepening and~~ cloud top height rising. ~~Generally~~In general, cloud streets form after traveling 15 km over open water. After 20 km, this formation enhances cloud cover to just below 100 %. After around 30 km, precipitation forms, though for the weaker event,

the development of precipitation is shifted to larger distances. ~~For the stronger event, we detect riming for cloud temperatures below -20°C. The variability of rime mass has the same horizontal scales as~~ Within our analysis, we developed statistical descriptions of various parameters (i) within the roll circulation ~~implying the importance of roll circulation on precipitation. The detailed observations of the two MCAO events could serve as a valuable reference for future model intercomparison studies.~~

and (ii) as a function of distance over open water. In particular, these detailed cloud metrics are well suited for the evaluation of cloud-resolving models close to the sea ice edge to evaluate their representation of dynamics and microphysics.

1 Introduction

Marine cold air outbreaks (MCAOs) are accompanied by strong air mass transformations. During Arctic MCAOs, cold and dry air flows from the ice-covered central Arctic southward over the open ocean. There, cloud streets form that are well visible in satellite images and transform to cellular convection downstream under extreme surface heat fluxes (Brümmer, 1996). ~~Especially over~~ Especially over the open ocean, cloud streets have important implications on the radiative surface energy budget due to their high albedo induced by liquid cloud tops (Geerts et al., 2022). Moreover, their long lifetimes affect precipitation evolution and characteristics (Morrison et al., 2012) and thus the Arctic water cycle. Arctic MCAOs can also strongly influence the weather in the mid-latitudes (Turner and Marshall, 2011).

~~Over sea ice, dynamical shear instability triggers mesoscale roll convection inside the atmospheric boundary layer (ABL) that is strengthened by thermal instability over open water (Atkinson and Wu Zhang, 1996). The strong roll circulation, called secondary flow, forms cloud streets aligned perpendicular to them (Brümmer, 1999). Within updrafts, clouds develop when moistened air ascends and reaches supersaturation. Within downdrafts, conditions are mostly cloud free as adiabatic heating causes evaporation of cloud particles. In the Arctic , cloud streets are often mixed-phase clouds (MPCs) that consist of supercooled liquid water mostly found at cloud top and precipitating ice particles below. If supersaturation~~ The Arctic is a hotspot with respect to ~~liquid is reached, liquid droplets will form and grow by condensation and ice particles will grow by vapor deposition (Morrison et al., 2012) after they formed from the liquid phase (Ansmann et al., 2008). In MPCs, ice will not grow by vapor deposition at the expense of liquid since the vapor pressure is mostly higher than the saturation pressure of ice and water (Korolev, 2007).Relevant ice growth processes in MPCs are aggregation and riming that are important as they determine precipitation.During riming, supercooled liquid droplets freeze on ice particles, which get larger and denser (Heymsfield, 1982; Erfani and Mitchell, 2017; Seifert et al., 2019). Nevertheless, riming rarely completely depletes liquid because it also reduces the number of iceparticles by precipitation. Riming can be enhanced in updrafts, which lift ice particles and expose them to supercooled liquid water over a longer period before precipitating (Fitch and Garrett, 2022). Riming has been observed frequently in Arctic MPCs (McFarquhar et al., 2007; Mioche et al., 2017), even when the liquid water path (LWP) is lower than $50\,\mathrm{g\,m^{-2}}$ (Fitch and Garrett, 2022). Large Eddy Simulations~~ climate change, most pronounced by strong surface temperature increases and sea ice decline (Wendisch et al., 2023). Dahlke et al. (2022) also showed significant shifts in the occurrence of MCAOs, i.e., decreases in early winter and increases in late winter, possibly caused by changes in

synoptic circulation patterns and feedbacks involving the retreating sea ice. How MCAO characteristics will develop in the future will require improved modeling capabilities (Geerts et al., 2022) and a better process understanding of these air-mass transformations, including cloud phase changes (Pithan et al., 2018). To resolve the mesoscale cloud organization in MCAOs, large-eddy simulations (LES) ~~by Tornow et al. (2021) find riming highly relevant for preconditioning MCAO cloud regime transitions.~~

~~LES identified riming (Tornow et al., 2022), turbulent transport (de Roode et al., 2019), flow divergence, and sharpness of~~ are required, but especially the transition between organization states is difficult to model as initial conditions, turbulence, cloud microphysics, and large-scale flow interact. Furthermore, small-scale surface heterogeneities in the marginal sea ice zone (MIZ) ~~(Spensberger and Spengler, 2021; Gryschka et al., 2008) as important factors for the transformation of~~ are important for the ~~convection regime within cold air outbreaks. Higher initial concentrations of cloud condensation nuclei delay precipitation formation (Tornow et al., 2021) and higher cloud droplet number concentrations slow down transformation to open cells, reduce LWP, and enhance amount of precipitation (de Roode et al., 2019). A larger amount of ice nucleating particles (INPs) increases the ice content of clouds, which might enhance riming and thus precipitation (Abel et al., 2017; Tornow et al., 2021). However, while a sharper MIZ increases surface heat fluxes, it seems not to affect precipitation amount in contrast to convergences (Spensberger and Spengler, 2021). Furthermore, model~~ formation of rolls (Gryschka et al., 2014) whereby the exposure of air to open water in the MIZ plays an important role (Spensberger and Spengler, 2021). LES studies also highlighted the importance of mixed-phase microphysical processes in preconditioning the transition of cloud organization (Abel et al., 2017; Tornow et ~~. Model~~ settings like the employed ice microphysical scheme and model resolution affect the timing of transformation that differs between the models~~(de Roode et al., 2019). Cloud cover decreases~~, e.g., when the ice phase is permitted (de Roode et al., 2019), while a higher resolution evokes roll convection at smaller ~~fetches~~ distances to the sea ice edge and increases precipitation amount (Spensberger and Spengler, 2021). However, no consensus has been reached ~~between different model studies yet.~~ and progress is delayed by the lack of observations to confront models.

~~A variety of measurements have been performed to gain a better understanding of MCAOs. The theoretical framework about the secondary flow and geometrical cloud parameters in arctic and tropical (Kuettner, 1971) MCAOs mostly builds on~~ First airborne in situ measurements ~~of the thermodynamic state inside the ABL. Examples for these Arctic campaigns are~~ during the Convection and Turbulence (KonTur) experiment (Markson, 1975; Brummer et al., 1982; Brümmer et al., 1985), ARKTIS '88 (Brümmer et al., 1992), '91, and '93 (Brümmer, 1999), and ~~the~~ Marginal Ice Zone Experiment (MIZEX; Walter and Overland, 1984) ~~. The influence of the warm ocean on the development of the ABL conditions and cloud/circulation morphology was analyzed by~~ investigated the mesoscale roll convection inside the atmospheric boundary layer (ABL) that is strengthened by thermal instability when air flows from the sea ice over the open water (Atkinson and Wu Zhang, 1996). Brümmer (1996) and Müller et al. (1999) ~~. They showed that the distance to~~ showed how the ABL was modified as a function of distance from the sea ice ~~edge characterizes~~ within the first 300 km under the influence of strong surface heat fluxes from open water. ~~When additionally considering open water in the MIZ and over leads, the total distance over open water is called fetch (Spensberger and Spengler, 2021). Variable initial sea ice conditions and convergence of the large-scale flow (Brümmer, 1996) might lead to variable cloud street characteristics across the streets at a specific fetch (Müller et al., 1999).~~

~~The transformation of roll to cellular convection has been studied in recent campaigns like the Cold-Air Outbreaks in the Marine Boundary Layer Experiment (COMBLE) . During COMBLE, remote sensing and in situ observations measured different stages of cloud development at two ground stations more than 1,000 km away from~~ While cloud reflectance measurements by satellites have provided important insights into the geometrical appearance of MCAOs since their beginning, their quantitative use was pioneered by Murray-Watson et al. (2023) who studied cloud development in a quasi-Lagrangian way. Using back trajectories, they investigated cloud properties derived by the Moderate Resolution Imaging Spectroradiometer (MODIS) as a function of time since the air passed the sea ice ~~(Geerts et al., 2022). Shipborne measurements, e.g. , the Iceland Greenland seas Project (IGP) , enable the characterization of convection over time periods longer than research flights (Duscha et al., 2022). The evolution of snowfall rates during MCAOs retrieved from CloudSat Cloud Profiling Radar (CPR) observations were studied by Mateling et al. (2023). However, according to Schirmacher et al. (2023), the accuracy of these CPR precipitation amounts is limited at the surface due to the blind zone, and poor spatial and temporal resolution of the CPR, which is especially important~~ edge. Liquid water path (LWP) and cloud top height (CTH) increase within the first 10 hours, with the strongest increase in the initial MCAO phase ~~when the ABL lies inside the blind zone.~~

~~Lately, the transformation was studied in a pseudo- and quasi-Lagrangian way by computing back trajectories. Focussing on liquid cloud evolution concerning outbreak strength and aerosol concentration, Murray-Watson et al. (2023) retrieved the time since an air mass passively sensed by a satellite passed the sea~~ , i.e., the first couple of hours. Further, they demonstrate that MCAO strength affects the development until 30 h after the air left the ice edge. However, ~~no mixed-phase clouds were considered due to satellite limitations. To characterize the thermodynamic evolution prior to a MCAO event, Dahlke et al. (2022) combined radiosoundings of the same air mass at Ny-Ålesund and RV *Polarstern* during the Multidisciplinary drifting Observatory for the Study of Arctic Climate (MOSAiC) experiment. Not only case studies but also trends of the strength and location of Arctic MCAOs were conducted based on reanalysis data (Papritz and Spengler, 2017; Dahlke et al., 2022). Diminishing sea ice extend,~~ due to retrieval limitations, they only considered liquid-dominated clouds and no information on vertical structure and precipitation is available. The important role of snowfall by MCAOs, producing the majority of snowfall in the North Atlantic, was shown by Mateling et al. (2023) using Cloudsat radar observations. However, Cloudsat sampling is limited by its blind zone of 1 km (Maahn et al., 2014; Schirmacher et al., 2023) and it is unclear whether differences to model precipitation (von Lerber et al., 2022) result from model deficits or instrument limitation.

In summary, there is a clear need for high-resolution cloud observations within MCAO, which are typically only available from ground-based remote sensing measurements at supersites. Therefore, the Cold-Air Outbreaks in the ~~induced changes in atmospheric dynamics (Dahlke et al., 2022), and clouds (Klingebiel et al., 2023) might lead to strong MCAOs at locations where they did not occur so far.~~

~~Despite recent advances in MCAO understanding, a better understanding of microphysical processes is needed to improve numerical simulations of past, present, and future MCAOs. In particular, it is important to disentangle the roles of local and large-scale influences on roll circulation evolution. However, the difficulty in resolving the initial MPC conditions remains when using satellite observations that cover large distances. Spatially fine resolved observations across multiple cloud streets, particularly close to~~ Marine Boundary Layer Experiment (COMBLE) in 2021/2022 (Geerts et al., 2022) established two ground

stations at Andenes and Bear Island, Norway, which provided important insights into cloud properties (Mages et al., 2022; Lackner et al., 20

130 and supported model evaluation (Geerts et al., 2022). However, these stations were located about 1000 km away from the sea ice ~~, exist only rarely for cloud macrophysical properties and , to our knowledge, not at all for cloud microphysical properties and precipitation.~~ . Thus, only open and closed cellular convection but no cloud streets have been observed.

~~This study analyzes high-resolution airborne remote sensing and collocated in situ observations of MCAOs~~ In this study, we exploit detailed cloud observations taken during the initial MCAO phase close to the ~~sea ice , where conditions strongly shape~~

135 ~~further downstream MCAO development . Dedicated flight patterns sampled repetitive crosssections through cloud streets on two days~~ ice edge, where rapid development of mixed-phase clouds occurred. We use airborne remote sensing observations that target model evaluation in a statistical sense and suggest suitable metrics for this. The measurements were performed during the HALO-(AC)[3] ~~(High Altitude and LOng range research aircraft - ArctiC Amplification: Climate Relevant Atmospheric and SurfaCe Processes, and Feedback Mechanisms; Wendisch et al., 2021) campaign in March/April 2022. Trajectory calculations~~

140 ~~allow us to analyze ABL and cloud development, precipitation onset, and riming in a pseudo-Lagrangian way, i.e. , as a function of fetch. The focus is on the initial development within the first 170 km fetch. We aim to resolve the variability of meteorological parameters that is unresolved in grid boxes of reanalyses and numerical weather predictions, and even in satellite observations like the~~ campaign (Wendisch et al., 2024) that took place over the Fram Strait where MCAOs occur frequently (Dahlke et al., 2022; Mateling et al., 2023; Papritz et al., 2015). We focus on a major MCAO that remained active

145 for more than two weeks (Walbröl et al., 2024). Within this period of northerly flow, just three days apart, two dedicated research flights were performed with active and passive remote sensing instrumentation. The environmental situations during the flights have many commonalities but slightly different flavors, in particular with respect to the cloud properties. Strait flight tracks crossed cloud streets perpendicular to their elongated orientation multiple times to perform high-resolution measurements of cloud and precipitation properties which are not possible from satellite, e.g., see LWP ~~from the Moderate~~

150 ~~Resolution Imaging Spectroradiometer (MODIS ; Fig.1a, b; red box in (b) compared to (d)). The area of interest is the Fram Strait since most strong MCAOs in the Nordic Seas occur west of Svalbard (Papritz and Spengler, 2017).Contrarily to previous flight strategies, our flight paths cross the cloud streets perpendicularly and, thus, go along the secondary flow to enable its investigation. To investigate the phase composite of MPCs, we use remote sensing observations taken from above clouds, which resolve the liquid layer at cloud top best. With an averaged rime fraction of 87~~observations by MODIS (Fig. 1c, d).

155 The data cover a fetch, i.e., the distance the air traveled over open water prior to the measurement, up to about 150 ~~%, Maherndl et al. (2023b) showed that riming is a key process during the full HALO-(AC)[3] campaign when remote sensing and collocated in situ observations were obtained. Thus~~km. From these unique measurements, we aim to answer the ~~open question of how riming depends on fetch and how it relates to the roll convection for the two case studies.~~following questions:

I. What are the differences between the environmental conditions on both flight days, and what are their implications on

160 cloud development?

II. Can we identify characteristic changes in cloud and precipitation properties perpendicular to cloud street orientation, i.e., within the roll circulation?

165 The paper is organized as follows: First, we introduce the airborne ~~instruments and data, as well as auxiliary spaceborne and reanalysis~~ measurements and data (Sect. 2). Second, we describe ~~our methodology : the calculation of fetch for observations from~~ the methodology that we developed to assign the fetch to each measurement using back trajectories (Sect. 3.1) and the identification ~~of~~ algorithm to detect roll circulations from ~~radar reflectivities~~ cloud radar measurements (Sect. 3.2). Section 4 ~~answers the following questions: Which thermodynamic conditions characterize the two MCAO events (See~~ describes boundary

170 layer and cloud development during the two flights (Sect. 4.1)~~? Which cloud properties are associated with~~, characterizes cloud properties within roll circulation (~~See~~Sect. 4.3) ~~? How do circulation and cloud properties change with fetch in the initial state of MCAOs and when do cloud streets start to precipitate (Sec. 4.4)? What is the impact of riming on MCAO transformation? (Sec. 4.2) The findings are synthesized to describe the interaction between roll circulation, cloud macro-, and microphysics (Sect. ??)~~and the development along fetch (4.4). Finally, Sect. 5 concludes ~~the study and discusses future steps~~on the questions

175 raised above and discusses pathways for future model evaluation.

2 Data

~~In this study, airborne~~ Airborne measurements from the HALO-(AC)[3] campaign (Wendisch et al., 2021) ~~are analyzed.~~ build the backbone of this study. During this campaign, the High Altitude and LOng-range research aircraft (*HALO*; Ziereis and Gläßer, 2006), the research aircraft *Polar 5* (*P5*) and *Polar 6* (*P6*; Wesche et al., 2016) operated in the North Atlantic sector of the

180 Arctic at altitudes around 10 km, 3 km, and below 3 km, respectively. This analysis mostly focuses on radar, radiometer, lidar, and dropsonde measurements from *P5* that probed MCAO events in their early phase. Dropsonde measurements from *HALO* and in situ observations from *P6* further support the analysis. We limit the analysis to measurements taken over ocean and restrict the remote sensing measurements to straight flight segments that exceed a flight altitude of 2 km ~~observing~~ to observe clouds from aloft. The focus lies on two ~~MCAO events~~*P5* flights, namely on 01 April 2022 (Fig.~~1c) and on~~ 1a) and 04 April

185 2022 (Fig.~~1d), during which cold air was advected from the sea ice over the Fram Strait leading to the formation of cloud streets. On 04 April, a convergence line also appeared in the Fram Strait's center. Since we aim to investigate the influence of varying meteorological conditions on roll circulation, we analyze both case studies, which show slightly varying environmental conditions~~ 1b). To investigate the roll circulation, the flight paths crossed the cloud streets perpendicularly. *P5* probed along the same path back and forth, yielding 6 legs on 01 April (09:08–14:20 UTC) and 4 legs on 04 April (10:06–14:22 UTC).

190 ~~Categorization of P5 airborne data. daydescriptioncolorlocation01 Aprilinfluence by Svalbardredlongitude>9.08°E01 Aprilprior to cloud streetsgreenfetch<15 km~~

2.1 Synoptic overview of cases

On 01 ~~Aprilcloud streetsblueremaining data04 Aprilinfluence by Svalbard and convergence lineredlongitude>3.7°E04 Aprilprior to cloud streetsgreenlongitude<1.7°E~~and 04 April~~cloud streetsblueremaining data~~

the large-scale constellation with a high-pressure system over Greenland and a low-pressure system over Siberia led to the advection of cold air from the central Arctic over the open ocean (Fig. 1a, b) and to cloud street formation (Fig. 1e, f). On 01 April, the center of the cold air at 850 hPa was located over Svalbard. A local near-surface low-pressure system southwest of Svalbard resulted in a near-surface north-easterly flow. With height, the flow turned northerly as indicated by the 500 hPa geopotential (Fig. 1a). On 04 April, contrarily, the cold air at 850 hPa height was shifted more to the west, and the flow at all heights aligned parallel to the sea ice edge over the Fram Strait (Fig. 1b). The easterly flow forced air to ascend over Svalbard, causing a lee effect. Therefore, a larger cloud-free region west of the island appeared, and a convergence line parallel to the ice edge at the transition to the cloudy regime is visible (Fig. 1f). However, note that the flow within our study area might deviate from the large-scale condition. On both days, the MCAO index was stronger than the 75th percentile of the climatology from 1979 to 2022 (Walbröl et al., 2024). While the synoptic conditions are similar for both cases, however, differences in flow directions lead to different MCAO strengths that precondition the evolution over water.

2.2 Airborne instrumentation

Dropsondes: Vaisala Dropsondes RD94 were launched from *P5* and *HALO*. From *P5*, 18 and 14 sondes were launched on 01 and 04 April, respectively. They provide vertical profiles of potential temperature (θ; accuracy=0.2 K), relative humidity (2 %), pressure (0.4 hPa), and horizontal wind components derived from GPS recordings (Vaisala, 2010; George et al., 2021).

Airborne Mobile Aerosol Lidar (AMALi): AMALi onboard *P5* measures profiles of backscattered intensities at 532 nm (parallel and perpendicular polarized) and 355 nm (not polarized; Stachlewska et al., 2010). The lidar measurements are processed with a vertical resolution of 7.5 m and temporal resolution of 1 s. Lidar backscatter is highly sensitive to hydrometeors, especially to liquid, which, in our case, is always super-cooled. Cloud top height (CTH) is obtained for every profile that has consecutive heights with backscatter coefficients exceeding one of cloud-free sections by a factor of five. The CTH is the maximum altitude of these consecutive heights. Further details can be found in Mech et al. (2022a) and Schirmacher et al. (2023).

Microwave Radar/radiometer for Arctic Clouds (MiRAC): The active component of the downlooking airborne MiRAC (Mech et al., 2019) onboard *P5* consists of a frequency-modulated continuous wave (FMCW) radar that operates at 94 GHz. Additionally, an 89 GHz passive channel accompanies the active measurements. Both measurements are taken with 25° backward

inclination of the instruments. While the vertically resolved radar measurements are reconstructed to nadir measurements, the passive measurements represent a slant path. MiRAC measures every second, which corresponds to a horizontal resolution of the equivalent radar reflectivity (Ze) of about 85 m at the ground in flight direction for a typical cruise altitude of 3 km height and ground speed of 80 m s^{-1}. The radar measurements are quality controlled and corrected for ~~the 25° backward inclination of the instrument,~~ surface clutter, and aircraft attitude (Mech et al., 2019). The sensitivity and vertical resolution of the cloud radar depend on the ~~setting~~chirp settings. During HALO-(AC)[3], the detection limit for the most distant ranges from $P5$ of 3 km ~~from $P5$~~ was around -45 dBZ and the vertical resolution was 4.5 m close to the aircraft and at most 13.5 m (Mech et al., 2022a). The processing interpolated the vertical resolution to 5 m over the whole profile. A blind zone of 150 m above ground is omitted due to ground clutter (Schirmacher et al., 2023). The accuracy of Ze is about 0.5 dBZ. Attenuation by water vapor (<1 dBZ) and clouds (~0.6 dBZ) can potentially reduce this accuracy (Schirmacher et al., 2023). ~~For some profiles , the radar detects several cloud layers~~

Cloud top height is also derived from the radar profiles at the height of the uppermost radar reflectivity signal above the noise level. Comparing this height with CTH from lidar allows us to assess the supercooled liquid layer thickness (LLT). Here, we exploit the fact that the lidar is more sensitive to particle amount (liquid), whereas the radar is more sensitive to particle size, i.e., ice particles (Ruiz-Donoso et al., 2020). Due to limited vertical resolutions of the instruments and resulting uncertainties in CTH, the CTH of the lidar has to exceed the CTH of the radar by at least 10 m to be defined as liquid topped and thus mixed-phase. For the calculation of hydrometeor depth (D), we take the difference between lidar CTH and the lowest radar signal within a continuous cloud layer. However, ~~we focus only on the highest cloud layer and do not differentiate between multilayer clouds in the analysis.~~ if a minor gap in the cloud profile occurs, i.e., the vertical distance between two layers is smaller than 50 m we define only one layer from the lower cloud bottom to the upper cloud top.

We define profiles containing a Ze value higher than -5 dBZ (Schirmacher et al., 2023) in the lowest 500 m (Shupe et al., 2008) as precipitating. Using the Ze-S relation for three bullet rosettes (Kulie and Bennartz, 2009), this value corresponds to a snowfall rate (S) of 0.07 mm h^{-1}. This relation is also used to analyze S close to the ground at 150 m. Note that these S estimates are inaccurate since Z-S relations highly depend on ice habits, which are very variable within cloud streets (Maherndl et al., 2023a; Moser et al., 2023).

The passive channel observes brightness temperatures (TB) primarily influenced by the emission of liquid clouds and the surface. Differences in TB for clear-sky and cloudy situations are used to retrieve LWP over ocean via a regression approach (Ruiz-Donoso et al., 2020). ~~Its sensitivity is below 5 g m^{-2} and the absolute accuracy~~ Due to the unknown emissivity of sea ice, LWP is only calculated over open ocean. Depending on atmospheric conditions, the maximum uncertainty is below 30 g m^{-2} (Ruiz-Donoso et al., 2020). While radar reflectivities are corrected to nadir profiles, the ~~LWP is derived from slanted TB measurements (Mech et al., 2022a). Because of the liquid layer at cloud top , the LWP signal of MPCs is mostly from~~ and thus LWP measurements are along the slant path (Mech et al., 2022a). As shown by the lidar backscatter and its strong attenuation close to cloud top and in accordance with Shupe et al. (2008) we assume that most liquid resides in the uppermost few hundred meters of the ~~clouds. Due to variable cloudtop heights ($CTHs$)~~cloud. Therefore, LWP lags behind the radar observation in ~~a non-constant matter. However, based~~ time. Based on geometric considerations, we shift the LWP

8

measurements assuming a daily average CTH for cloud streets. Since this average differs for both days, we shift the LWP measurements by different time periods, i.e., 16 and 19 s on 01 and 04 April, respectively, having an estimated maximum error of 4 s. As a result, a good agreement between LWP peaks coincide with and profiles of high Ze (Fig. 2a, d). Visualization of cloud circulation identification. Time series (30 s) of the equivalent radar reflectivity Ze profiles measured by MiRAC starting at 10:08:43 UTC on 01 April (a), Ze at an altitude of 0.7 of the normalized hydrometeor depth (b, step III), and after further averaging over 3 s (c, step V). The detection of maxima (dark blue, step VI) and minima (light blue, step VII) is described in Sec. 3.2. The prominence (c, vertical orange line) and width of the peak (c, horizontal orange line) are important parameters for the peak detection. Note that Ze is shown in logarithmic space while peaks are detected in the linear space. Time series of liquid water path (LWP, 25° back inclination) shifted by 16 s to match nadir-looking Ze observations for clouds with a cloud top height of 1 km (d). For comparison, the cloud top height observed by the lidar AMALi is displayed (a, black dots). The shown time period covers fetches from 73 to 80 km and corresponds to a flight distance of 7 km.

Airborne Mobile Aerosol Lidar (AMALi): AMALi onboard *P5* measures profiles of backscattered intensities at 532 nm (parallel and perpendicular polarized) and 355 nm (not polarized; Stachlewska et al., 2010). With a vertical resolution of 7.5 m, the CTH is obtained for every profile that has consecutive heights with backscatter coefficients exceeding the one of cloud-free sections by a factor of five. The CTH is the maximum altitude of these consecutive heights. Further details can be found in Mech et al. (2022a) and Schirmacher et al. (2023)can be observed.

In situ probes: The *P6* was equipped with three in situ probes, namely the Cloud Droplet Probe (CDP; Lance et al., 2010), Cloud Imaging Probe (CIP; Baumgardner et al., 2011) and Precipitation Imaging Probe (PIP; Baumgardner et al., 2011). The CDP is a forward-scattering optical spectrometer that measures small cloud particles (2.8–50 μm). Larger cloud particles are observed by the CIP (15–960 μm) and PIP (103 μm–6.4 mm) that record shadow images of the cloud particles as the particles pass through the sampling area (Moser et al., 2023). By combining CDP, CIP, and PIP, a A continuous particle size distribution is derived for calculating rime mass by combining CDP, CIP, and PIP. The CIP and PIP data are processed similarly to previous campaigns (Mech et al., 2022a).

Collocation: On both days, *P5* (remote sensing) and *P6* (in situ) were closely collocated. For the analysis of riming, we use a data subset during which both aircraft flew on straight paths with a time difference between the collocated measurements of less than 5 min, a spatial distance between both platforms below 5 km, and a flight altitude of *P6* between 0.15 and 1.3 km. With this, we reduce the error caused by sampling different air masses with *P5* and *P6* and also by sampling air masses with varying microphysical properties due to changing *P6* locations within the cloud vertical extent. On 01 April, 3971 seconds of collocated observations cover longitudes between 4.5 and 6.5°E corresponding to 25–165 km fetch. On 04 April, only 845 seconds of observations are collocated that are located between 1.5 and 4.5°E and cover fetches between 55 and 165 km, mostly at around 80 km. On 01 April, seven collocated data segments exist with gaps of less than 5 s. These segments cover 39 min at 60–140 km fetch with most measurements concentrated around 7°E longitude.

2.3 Satellite and reanalysis data

For the sea ice concentration (SIC), we use a daily product that merges satellite observations from MODIS and the second Advanced Microwave Scanning Radiometer (AMSR2) at 1 km horizontal resolution (Ludwig et al., 2020). For the analysis, we interpolate the data to a 0.05° x 0.05° latitude/longitude grid. Sea surface temperatures (SST) are obtained from the Arctic Ocean - Sea and Ice Surface Temperature product based upon observations from the Metop–A Advanced Very High Resolution Radiometer (AVHRR). The daily product (Copernicus Marine Service, 2023) has a spatial resolution of 0.05° and covers surface temperatures of ~~the~~ ocean, sea ice, and MIZ. Using satellite SST and dropsonde temperature measurements above open water (Fig. ~~1e, f~~ 1g, h, black and white dots), we calculate the ~~MCAO~~ MCAO index from the difference between the potential temperature (θ) at the sea surface and 850 hPa altitude. Generally, the ~~MCAO~~ MCAO index is positive during a MCAO and describes its strength (Papritz et al., 2015; Kolstad, 2017). ~~To compute back trajectories using Lagranto (Sprenger and Wernli, 2015), we use the three-dimensional wind fields of the~~ Over ocean, we moreover calculated surface heat fluxes from the satellite SST data and dropsonde observations at 10 m height based on the Coupled Ocean-Atmosphere Response Experiment (COARE) bulk air-sea flux algorithm (Fairall et al., 2003). European Centre for Medium-Range Weather Forecasts (ECMWF) reanalysis product version 5 (ERA5; Hersbach et al., 2020) ~~. This product~~ is used to analyze the large-scale environmental conditions and to compute back trajectories using Lagranto (Sprenger and Wernli, 2015). ERA5's temporal, horizontal, and vertical resolution is one hour, 31 km, and 137 model levels from the surface up to the top of the atmosphere, respectively (Kirbus et al., 2023). Note, that most HALO dropsondes have been assimilated in ERA5, leading to an improved performance for our study cases.

3 Analysis and identification approaches

In the following, we describe two approaches we established for analyzing airborne measurements. The first concerns the quantification of the fetch assigned to each measurement (Sect. 3.1). Second, we present a novel method to identify roll circulation from airborne radar reflectivities only (Sect. 3.2).

3.1 Trajectory calculations and fetch

~~The~~ During MCAOs, the warm ocean alters ~~the ABL conditions~~ thermodynamic conditions of airmasses within the ABL, which were formed in the central Arctic, by turbulent surface heat and moisture fluxes (e.g., Brümmer, 1996) ~~. The thermodynamic profile of an airmass formed in the central Arctic flowing southward is modified by strong turbulent surface fluxes evident~~ whenever SIC is below 100 % ~~even if no clouds develop.~~ . We aim to quantify this influence of open water on ~~the~~ ABL development. ~~The distance of an air parcel to sea ice edge has been used to characterize the exposure to open water (Brümmer, 1996; Müller et al., 1999). However, this distance does not capture the influence of MIZ and leads encountered in the ice. We account for all areas of open water , which was already done in the past by either calculating the fetch (Brümmer, 1996; Müller et al., 1999; Spensberger and Spengler, 2 or travel time (Tornow et al., 2021; Murray-Watson et al., 2023).~~

~~Turbulent fluxes are proportional to wind speed. Stronger fluxes supply more heat/moisture, affect higher altitudes, and, thus, modify the atmosphere more. If winds of different strengths advect an air mass over a constant fetch, the integrated flux will be roughly constant for both scenarios since the shorter travel time counteracts the stronger fluxes for the higher wind speed. If~~
~~winds of different strengths advect an air mass for a constant time, the instantaneous fluxes, integrated flux, and fetch increase for the higher wind speed. Therefore, the integrated flux depends on wind speed similar to fetch as opposed to travel time . Hence, we calculate fetch for each airborne measurement to quantify the influence of open water .~~

~~In this study, however, the flow is slowed to an extent that discrepancies between travel time and fetch emerge only over land~~Since it is impossible to calculate integrated surface fluxes along the trajectories with our data, we derive the fetch for each airborne measurement. We follow Spensberger and Spengler (2021) and also account for open water over the MIZ and leads in the ice. For flows unaffected by land masses, travel time over open water and fetch can be linearly converted and are both valid to study. The correlation coefficient between ~~the travel time over open water~~ travel time and fetch is 0.99 for all *P5* measurements that are not influenced by land masses and -0.5 for *P5* ~~measurements that are~~measurements influenced by Svalbard. ~~For wind flows unaffected by land masses, integrated travel time and fetch should be linearly convertible and both parameters are valid to study~~Therefore, the latter data have been removed from the analysis (see below).

~~To calculate fetch, we~~ We need to know the air masses' previous path to calculate fetch for each measurement. For this purpose, we compute near-surface Lagrangian back trajectories using Lagranto (Sprenger and Wernli, 2015) with ERA5 wind fields as input. ~~ERA5 captures ABL conditions well, e.g., it represents the course of the ABL height evolution along the flight path similarly to radar observations even though it overestimates the absolute values by roughly 200 m (not shown).~~ Specifically, we calculate back trajectories for the previous 12 hours for every flight minute and ~~resample them to one second~~assign them to the observations within each minute. The trajectories originate at the horizontal location of *P5* and at 1000 hPa height corresponding to roughly 300 m above the surface. To investigate the influence of the surface on the air masses, we take a near-surface starting point for the trajectories. Similar to Spensberger and Spengler (2021), we calculate the fetch for every back trajectory ~~from the ERA5 wind field~~ by integrating the ratio of open water obtained from MODIS-AMSR2 SIC data (Sect. 2.3) along the back trajectory paths over the previous 12 h until measurement time (0 h~~; see Appendix ?? for error estimation~~):

$$fetch = \int\limits_{s(12h)}^{s(0h)} (1 - SIC(s))ds \tag{1}$$

Note that due to the resolution of ERA, neighboring trajectories are rather similar (Fig. 1g, h). Differences in fetches between two neighboring trajectories mainly come from differences in SIC along the trajectories. The median of the relative change between two adjacent fetches is 9.6 %.

To concentrate on cloud street characteristics during undisturbed MCAO conditions, we limit the analysis to data that did not pass Svalbard at any time and that are not affected by the convergence line on 04 April (~~Tab.~~ Table 1; Fig. 1, non-red dots). The remaining measurements are classified to be either 'cloud streets' (Fig. 1, blue) if radar reflectivities appear regularly or 'prior to cloud streets' (Fig. 1, green~~; Tab. 1~~). The latter category includes samples taken over and close to sea ice that have fetches less than 15 km on 01 April and longitudes smaller than 1.7°E on 04 April (fetches of about 17 km; Table 1). On 04

Table 1. Categorization of *P5* airborne data.

day	description	color	location
01 April	influence by Svalbard	red	longitude>9.08°E
01 April	prior to cloud streets	green	fetch<15 km
01 April	cloud streets	blue	remaining data
04 April	influence by Svalbard and convergence line	red	longitude>3.7°E
04 April	prior to cloud streets	green	longitude<1.7°E
04 April	cloud streets	blue	remaining data

360 April, longitude instead of fetch is used for classification because cloud streets over open ocean and cloud-free conditions over sea ice have both fetches of 17 km. Note that fetch includes contributions from the MIZ (80 % <SIC> 100 %) and open water. ~~Due to the low amount of data that have variable fetches due to different fetches over MIZ only, it is impossible to disentangle the influence of MIZ.~~

3.2 Roll circulation identification

365 To identify roll circulations from radar measurements, we must rely on indirect information. Previous studies applied spectral analysis to observations of the three wind components, temperature, mixing ratio, and radiative fluxes (Brümmer et al., 1985, 1992; Brümmer, 1999; Walter and Overland, 1984). While vertical velocity cannot be extracted from the airborne Doppler measurements (Mech et al., 2022a), we exploit the fact that due to the vertical motion, cloud particles form to the largest extent at the location of the strongest updraft~~if they are not influenced~~. Here, frequent saturation with respect to ice and

370 thus the formation of cloud droplets and growth of both liquid and ice particles occurs (Korolev and Field, 2008). In order to account for potential influences by dry entrainment at cloud top (Klingebiel et al., 2015) or precipitation (Morrison et al., 2012) ~~. This leads to a maximum in the radar signal. We solely use $Ze_{0.7}$, which is the radar reflectivity~~ we only consider measurements at the height of 0.7 of the hydrometeor depth (D~~, the difference between CTH and lowest radar signal height per profile)~~ ~~. In this way, $Ze_{0.7}$ serves as a proxy for vertical velocity, and we assume that maxima in~~ ; Sec. 2.2) for the identification. By

375 using the radar reflectivity at this height ($Ze_{0.7}$~~represent updraft and minima downdraft regions of the roll circulation.~~

~~Relative occurrences of Ze that exceed -5 dBZ and are above 500 m height (a). Relative occurrence of precipitation (b, dashed) and minimum Ze of each radar profile (b, solid) as a proxy for dry entrainment accumulated with height. The y-axis is the normalized hydrometeor depth (0=base, 1=top). The height that is used to identify roll circulations is indicated by the red line. We take Ze at the height of 0.7 of D to~~), we target the largest ice particles within the profiles and minimize the influence

380 of dry air entrainment/supercooled liquid water droplets at cloud top and precipitation at the bottom of D. ~~Precipitation is assumed to occur at Ze values larger than -5 dBZ (Schirmacher et al., 2023) that are below 500 m height (Shupe et al., 2008) . Figure A1 explains the choice of this height (red line): here, non-precipitating large ice particles ($Ze > $ -5 dBZ, height > 500 m) are most frequent with 29 % (Fig. A1a) and with 98 %, most precipitation occurs below that height level (Fig. A1b,~~

385 ~~dashed). Dry entrainment and liquid droplets seem rare at that height since 91 % of the lowest Ze per profile lie above the altitude of 0.7 of D (Fig. A1b, solid). In conclusion, we take Ze~~ See Appendix A for a discussion about the height selection and a sensitivity analysis.

$Ze_{0.7}$ serves as a proxy for vertical ~~motion at a height mostly consisting of large ice particles and is least affected by entrainment and precipitation.~~

390 ~~To find up- and downdraft regions, we follow this recipe: Determine the hydrometeor depth (D) for every profile. Average Ze over 100 m in the vertical to reduce noise. Smooth Ze by averaging over 3 s to minimize noise detection. Retrieve the smoothed $Ze_{0.7}$ at 0.7 of D for each profile (Fig. 2c). Derive the large-scale background Ze_{back} by averaging $Ze_{0.7}$ over 500 s ($\sim$ 40 km). Determine peaks in $Ze_{0.7}$ using the python package scipy.signal.find_peaks (Virtanen et al., 2020).If Ze_{back} $\geq 0.67\,mm^6\,m^{-3}$, find peaks for~~ velocity, and we assume that maxima in $Ze_{0.7}$ ~~(Fig.2, dark blue) with a prominence of at least $0.5\,mm^6\,m^{-3}$ (difference between the height of the peak and its lowest contour line; vertical orange line) and a width~~

395 ~~of at least 2.9 samples (horizontal orange line). If $Ze_{back} < 0.67\,mm^6\,m^{-3}$, find peaks for~~ represent updraft regions, while minima in $Ze_{0.7}$ ~~with a prominence of at least $0.1\,mm^6$~~ represent downdraft regions of the roll circulation. For cloud-free areas, we define the downdraft in the area's center. The workflow behind the circulation detection is summarized in Fig. ~~m^{-3} and a width of at least 2.9 samples. Here, we apply two different thresholds depending on Ze_{back} since the magnitude of the averaged Ze and its peaks generally increase with fetch. Find the minimum~~ 2. See Appendix A for further details and Table

400 A1 for a sensitivity analysis. Among different configurations, we selected the detection algorithm with the best ratio between determining peaks and ignoring noise. This automated peak detection depends only on the large-scale condition and thus might not determine every maximum of $Ze_{0.7}$ ~~, which is not averaged over 3 s, between every two maxima (Fig. 2, light blue). If conditions between two cloud streets are cloud free, we consider the downdraft location at the center of the cloud-free distance.~~ considered by the human eye.

405 ~~Note that we can~~ We only apply the detection algorithm to the 'cloud street' regime as roll convection is ~~mostly too weak to evoke radar signals prior~~ invisible to the radar as long as no significant amounts of hydrometeors are present. According to our definition, the maximum updraft ~~, i.e.~~ (maximum $Ze_{0.7}$~~,~~) does not necessarily need to be centered between the two detected edges of our roll circulation object. The wavelength of the circulation (λ) is the distance between two identified adjacent downdrafts. The mesoscale circulation is described by the aspect ratio (AR), i.e., the ratio between λ and CTH at the ~~position~~

410 ~~of the identified maximum in $Ze_{0.7}$. We identified 364 and 109~~ updraft position. In total, we identified 356 and 112 cloud circulation objects in the 'cloud street' regime on 01 and 04 April, respectively.

~~We tested several configurations of the roll circulation detection algorithm (for details, see Table A1) and selected the one with the best ratio between determining peaks and ignoring noise. This automated peak detection depends only on the large-scale condition and thus might not determine every maximum of $Ze_{0.7}$ considered by human eye.~~

4   Variability of thermodynamic conditions and cloud street properties

In the following, we first investigate the ~~thermodynamic state of the ABL~~ boundary layer conditions (Sect. 4.1) ~~to characterize the environmental conditions. For the 'cloud street' regime, we~~ and the preconditioning by riming (Sect. 4.2). Afterward, we statistically analyze cloud morphological and microphysical properties within the roll circulations ~~(See~~for the 'cloud street' regime, (Sect. 4.3) ~~. Afterward, we investigate how roll circulations and thus cloud properties develop~~ followed by an assessment of cloud and precipitation properties as a function of fetch within the first 170 km (4 h) of the MCAO development (~~See~~Sect. 4.4).

~~For the microphysical analysis, we introduce two metrics: first, the supercooled liquid layer thickness (LLT), which is the difference in CTH measured by the lidar and radar. Here, we exploit the fact that the lidar is more sensitive to particle amount (liquid), whereas the radar is more sensitive to particle size (ice; Ruiz-Donoso et al., 2020). Due to limited vertical resolutions of the instruments (Sec. 2.2)and resulting uncertainties in CTH, the CTH of the lidar has to exceed the CTH of the radar by at least 10~~

4.1   ABL conditioning

First, we investigate how much the ABL conditions differ between the cases, including possible drivers. The influence of the ocean on the ABL through surface sensible and latent heat fluxes is more pronounced on 01 than 04 April (Fig. ~~m to be defined as liquid topped. Second, we define profiles containing a Ze value higher than -5~~3e, f). Dropsondes show maxima of 450 (225) ~~dBZ (Schirmacher et al., 2023) in the lowest 500W~~ m (Shupe et al., 2008) as precipitating. Using the Ze-S relation for ~~three bullet rosettes following Kulie and Bennartz (2009), this value corresponds to a snowfall rate (S) of 0.07~~m^{-2} for sensible (latent) heat fluxes. Over the MIZ, fluxes decrease, and the ratio changes to a higher contribution of the sensible heat flux due to less evaporation over sea ice as also found by Li et al. (2020). Along the whole flight track, ERA5 shows that the sensible heat flux decreases much faster with distance from the sea ice edge on 04 than 01 April (Fig. ~~mm~~3e, f), even though the oceanic conditions, i.e., SST, are similar (Fig. ~~h^{-1}~~3a, b). This indicates that the atmospheric conditions differ between the cases, which is especially confirmed for temperature by differences in MCAO fields (Fig. 3c, d). The MCAO index averaged over all dropsondes launched from P5 is with 8.6 K stronger on 01 than 04 April (Table 2). Note that ~~this is a rough estimate since in situ measurements show that the crystal shapes within cloud streets are very variable (Maherndl et al., 2023a; Moser et al., 2023). In this study, S is analyzed close to the ground at 150 m. The precipitation fraction denotes the ratio of the number of precipitating to all profiles.~~

4.2   ~~Thermodynamic evolution and cloud appearance~~

although the dropsondes on 01 April were launched further away from sea ice, ERA5 fields show roughly the same factor of two differences over both flight tracks. In general, the fluxes and MCAO indices from ERA5 correspond to dropsonde estimates, except over sea ice where ERA5 seems to overestimate the fluxes. However, the dropsondes resolve finer spatial structures in both parameters.

Table 2. Conditions during 01 ~~April~~ and 04 April. BLH ~~stands~~ and CTH stand for atmospheric boundary layer height, i.e., the inversion height of potential temperature, and cloud top height, respectively.

parameter	source	01 April	04 April
~~$MCAO$~~ MCAO index	dropsondes	8.6 K	4.6 K
cloud street orientation	MODIS	10°N	5°N
cloud street wavelength	MODIS	2 km	1 km
temperature at cloud top	dropsondes	<-20°C	-20 to -10°C
median cloud street CTH	radar	700 m	300 m
interquartile range of cloud street CTH	radar	530–790 m	250–375 m
BLH trend	dropsondes	4.5 m km^{-1}	2.9 m km^{-1}
mixing ratio trend within 100 km fetch	dropsondes	< doubling	> doubling
driver of wind shear	dropsondes	wind direction	wind speed
~~precipitating radar profiles~~ cloud street profiles with precipitation	radar	67 %	35 %
cloud street profiles with liquid-topped ~~radar profiles~~ clouds	radar and lidar	86 %	71 %

~~On 01 and 04 April, cold air was advected from the central Arctic over the Fram Strait. With an $MCAO$ index averaged over all dropsondes of 8.6 K, the first MCAO event~~ The cloud condition on 01 April is ~~stronger than the second one on 04 April (Table 2). On both days, the evolution of the $MCAO$ index obtained by ERA5 reanalysis follows the one of SST and~~
450 ~~the largest increase of the $MCAO$ index is at around 70 km fetch (Fig. 3a, b), which is twice the size of an ERA5 grid point.~~

~~On 01 April, the MODIS image shows~~ characterized by cloud streets with an orientation of about 10° to the north (Fig.~~1c~~ 1e, black line) and a wavelength of about 2 km with shorter distances between the separated streets close to sea ice. Note that ~~the coarsest spatial resolution of the used~~ this information is retrieved from MODIS sensors (bands 1, 3, and 4) ~~is~~ that have a spatial resolution of at least 500 ~~m. On 04 April, the MODIS image shows cloud streets with an orientation of 5° to north (Fig. 1d,~~
455 ~~black line) and a wavelength of about 1 km. Due to its topography, the off-land flow at 1000 hPa westward of Svalbard descends in the vicinity of the island, particularly on 01 April (Fig. 3c, d; red), and the lee effect affects air mass characteristics, e.g. , causing cloud-free conditions close to the island. On 01 April~~m. Close to the sea ice edge, the near-surface air ~~mass~~ of the 'prior to cloud streets' regime ~~subsides~~ shows weak subsidence (Fig.~~3c; green)~~ and of 3g, green track). For the 'cloud street' regime, the air ascends except for fetches between 75 and 120 km (about 7°E longitude; blue track) even though SST and ~~$MCAO$~~
460 ~~indices abruptly~~ MCAO indices increase (Fig.~~3a; blue). Here, air mass subsides~~ 3a, c). We suggest that this subsidence, which is visible over the whole atmospheric column (not ~~shown)~~thus we suggest that this subsidence is due to a wave effect provoked by the island. On 04 April, the air mass starts ascending at larger fetches compared to 01 April without a notable wave effect (Fig. 3d)~~show n), is provoked by a wave effect induced by Svalbard.

~~Averaged dropsonde profiles from *HALO* and *P5* of temperature (a, f), potential temperature (b, g), mixing ratio (c, h), wind~~
465 ~~direction (d, i) and speed (e, j) binned by fetch on 01 April (first row) and 04 April 2022 (second row). The shaded areas represent the standard deviation of each category. The color coding is inspired by the categorization shown in Table 1. On 01~~

The thermodynamic state of the ABL is described by mean profiles of dropsondes released from *P5* and *HALO* over sea ice

470   and open water~~during both days (Fig. 1e, f, diamonds). Generally, the temperatures within the lowest 1 km increase with fetch due to heating from below (Fig. 4a, f). The temperature profiles reveal the difference in air mass between both days~~. On 01 April, temperatures are lower than -20°C throughout all altitudes over sea ice (fetch <15 km) and for parts over open water ~~.~~ ~~On 04 April, contrarily, all temperature profiles below 2 km height lie within −20 to −10°C.~~

~~The potential temperature (θ) of the free troposphere is on average lower by about 5 K on 01 April compared to 04 April~~

475   ~~(Fig.4b, g). Over open water, aneutrally-stratified ABL develops due to strong sensible and latent heat fluxes from the ocean and turbulent mixing of near-surface air. Note, that ERA5 shows about twice as high fluxes on 01 April compared to 04 April. Generally, the boundary layer height (BLH), i.e., the inversion height of θ, increases with fetch. On 01 April, the averaged BLH increase rate over all fetches is much stronger than on 04 April (Table 2~~ 4a). Over sea ice, the surface layers~~that~~ , which are cooled from the ground, and the air above~~that~~ , which is warmed by subsidence, generally develop an inversion. Profiles

480   that were sampled by *HALO* dropsondes over sea ice ~~close to the ice edge on 01 April~~ exhibit a thin (< 250 m deep) ABL~~,~~ ~~while dropsondes cannot detect a BLH in the central Arctic (81.3–87.0°N) on 04 April as it is likely too shallow (not shown). The flow over more frequent areas of open sea ice or refrozen leads within the MIZ (Li et al., 2020) might deepen the ABL. The inversion is stronger over sea ice and weakens less with fetch on 04 April due to a layer of warm air above the BLH. This layer additionally evokes a second inversion over water~~ . Close to sea ice edge, the depth of the ABL, which is capped by a

485   low-level jet (Fig.~~4g, blue).~~

~~Over sea ice (fetch < 15 km)~~ , the 4e) and has a low water vapor mixing ratio (0.5 g kg^{-1}~~) indicates the background~~ ; Fig. 4c), is similar to over closed sea ice (Fig. 4b). The mixing ratio indicates the low background vapor concentration of the polar air mass~~on 01 April, which is slightly higher over all heights on 04 April.In the ABL~~. With 28°, wind direction is constant with height while the near-surface wind comes from 0°N regardless of surface properties (Fig. 4d). Over open water,

490   the temperatures and, thus, wind speeds within the neutrally-stratified ABL increase with fetch. The boundary layer height (BLH), i.e., the inversion height of the potential temperature θ, doubles within the first 100 km (Fig. 4b). Also, the mixing ratio increases with fetch due to ~~latent heat fluxes leading to slightly less and more than a doubling within the first 100 km on 01 and 04 April, respectively.~~strong surface heat fluxes and turbulent mixing of near-surface air.

~~With 28°, wind direction is constant with height on~~ On 04 April, the MODIS image shows cloud streets with an orientation

495   of 5° to the north (Fig. 1f, black line) and a wavelength of about 1 km. The air mass ascends at fetches larger than 60 km, i.e., larger fetches compared to 01 April (Fig.~~4d). On~~ 3h). A wave effect is notable within the region affected by the lee effect but not for the analyzed data west of the convergence line. Warmer temperatures on 04 April ~~, a shear from north wind at the surface to west wind exists over all heights, which is strongest at 0.4–1~~reveal a difference in air mass between both days: all temperatures below 2 km height lie within $−20$ to $−10$°C (Fig.4i) ~~. The near-surface wind on 01 April and boundary-layer~~

500   ~~wind on 04 April are more northerly, particularly over sea ice they reach 0° N. On both days, the wind speed increases towards surface before it declines towards the surface at around~~ 4f) and θ of the free troposphere is on average by about 5 K higher

compared to 01 April (Fig. 4b, g). Furthermore, the mixing ratio of the polar air mass is slightly higher at all heights (Fig. 4c, h). Even though a low-level jet exists at 200 m over sea ice as before (Fig.4e, j). On 4j), flow conditions differ compared to 01 April, wind speed increases with fetch, while on 04 April, it reduces by 5 m s⁻¹ over water at 0.4–1. A directional shear from northerly wind at the surface to westerly wind occurs at all heights, which is strongest at BLH (Fig. km height, which aligns with the airmass identification from the θ profiles. The wind inside the ABL follows an Ekman spiral caused by friction that is enhanced over sea ice. Generally, inflection points in the wind form roll circulation by shear instability 14° to the left of the geostrophic wind (Atkinson and Wu Zhang, 1996). On 01 and 4i). Although $HALO$ dropsondes cannot detect a BLH in the central Arctic (81.3–87.0°N) as it is likely too shallow (not shown), the capping inversion over the sea ice close to its edge is stronger. On 04 April, the cloud streets align 10 and 70° to the left of the geostrophic wind, respectively, due to additional convective instability. The observed cloud streets form along the wind direction averaged over the lowest 100this inversion weakens less with fetch compared to 01 April due to a layer of warm air above BLH. Together with about half as high ERA5 surface fluxes on 04 April (Fig. 3e, f), this results in a much weaker BLH increase rate averaged over all fetches (Table 2) and a reduction of wind speeds by 5 mas found by Puhakka and Saarikivi (1986). s⁻¹.

On both days, the radar profiles in the 'cloud street' regime frequently (93 %) exhibit clouds. The contoured frequency by altitude diagrams (Fig.5) reveal 5) reveals the different cloud and precipitation characteristics of cloud streets between the days: especially, CTH is twice as high on 01 than on 04 Aprilas indicated by the radar measurements. Furthermore, the mean Ze profile (black dots) is larger over at all heights. On 01 April, values larger than -5 dBZ, which are associated with the onset of snowfall, occur over all heights, while on 04 April even below 500 m, Ze rarely exceeds -5 dBZ. Thus, more profiles precipitate at all heights. The shorter the fetch on 01 than on 04 April (Table 2). On 01 April, April, the stronger is the decrease in the mean Ze slightly decreases profile close to the surface even stronger for small fetches (not shown). Thus, near-surface ice particles might experience stronger evaporation sublimation on 01 April , especially when the mixing ratio is comparably small . Hence, surface snowfall rates are overestimated if derived from higher altitudes (Schirmacher et al., 2023)and relative humidity with respect to ice below 100 % (not shown). On 04 April, Ze rarely exceeds -5 dBZ even below 500 m reducing the frequency of precipitation compared to 01 April (Table 2). Moreover, mean Ze increases towards the surface, indicating the ongoing growth process of ice particles. Most On both days, most cloud streets are liquid-topped (Table 2). For most of these clouds, the CTH is higher than for , which mainly have higher CTH than non-liquid-topped clouds , and the averaged Ze profile is larger over all heights on 01 April (Fig. ??). Stronger turbulence in liquid-topped clouds might lift particles higher and increase amount and size of ice particles (Morrison et al., 2012). (not shown).

In summary, the MCAO event is colder and drier case on 01 than on April is by a factor of two stronger than 04 April with higher $MCAO$ indices due to colder and drier air masses (Table 2). On both days, wind shear occurs by wind speed changes on 01 and direction changes on 04 April. On 04 April, strong changes in wind direction at 0.4–1Contradicting the MCAO index, air subsides close to the surface in the 'cloud street' regime at fetches around 100 km over open water result in a slower advection of warm and moist air from the direction of Svalbard. Thus, the strength of the temperature inversion above BLH decreases less with fetch over open water than on on 01 April due to a wave effect caused by Svalbard.

4.2 Preconditioning by riming

Ice growth affects the boundary layer evolution during MCAOs in several ways, e.g., by reducing cloud liquid water and triggering early and light precipitation, which then cools and moistens the air below the cloud (Tornow et al., 2021). To investigate whether riming preconditions cloud microphysics and precipitation characteristics are already in the initial state
540 of MCAO evolution, we evaluate the strength and variability of riming. In doing so, we use a subset of in situ and remote sensing data within the 'cloud street' regime during which $P5$ and $P6$ were collocated (Sect. 2). To determine the degree of riming, we calculate the normalized rime mass (M) defined as the rime mass divided by the mass of the size-equivalent spherical graupel particle. Following Maherndl et al. (2023b), two methods are applied. The combined method uses the closure of in situ particle size distributions and Ze simulations obtained from running averages of in situ particle size distributions over
545 30 s. The in situ method relates M to in situ particle shape measurements only. The results of both retrievals are comparable. However, since the collocation of $P5$ and $P6$ measurements might be inaccurate, we only show results from the in situ method for which no matching is necessary. Note that our definition of updrafts might bias the following findings.

Considering particles with $M > 10^{-2}$ as rimed, more rimed particles exist on 01 April (97 %) than on 04 April (80 %). The median M of $10^{-1.6}$ on 01 April ~~, which reduces the rate of BLH increase with fetch (Brümmer, 1996). Contradicting~~
550 ~~the $MCAO$ index, ERA5 indicates subsidence at the surface in the 'cloud street' regime at fetches around 100~~and $10^{-1.8}$ on 04 April (Fig. ~~km on~~ 6a) clearly reveals that riming is only significantly active in cloud streets on 01 April. In particular, normalized rime masses $M > 10^{-1}$ only exist on 01 April. On this day, cloud top temperatures are colder than or at the low end of temperatures within the dendritic-growth zone (DGZ; -20 to -10°C) and hence too cold for aggregation to be dominant (Chellini et al., 2022). On 04 April, contrarily, riming is not significant because cloud top temperatures lie within the DGZ that
555 favors aggregation.

The spatial variability of riming is investigated by linearly detrended and mean-centered power spectra of M obtained during seven collocated segments (Sect. 2). Edge effects are minimized by applying a Hann window for smoothing. Due to the units of variance, the power spectrum increases automatically for smaller wavelengths. The averaged power spectrum of M peaks at about 0.7 and 1.1 km (Fig. 6b). These values roughly correspond to the wavelength λ of cloud streets as seen in the MODIS
560 images (Fig. 1) and a more detailed comparison with λ detected by the remote sensing measurements will be performed in Sect. 4.4. For 01 April~~.~~, we suggest that riming is enhanced in updraft regions, where it results in higher precipitation rates. Thus, riming, which is only active during the strong MCAO case with cold temperatures, seems to precondition precipitation. We further analyze the effect of riming on cloud microphysics in the following sections.

4.3 ~~Impact of roll circulation on cloud properties~~

565 ## 4.3 Impact of roll circulation on cloud and precipitation properties

~~To characterize how up- and downdraft regions~~of the roll circulations affect cloud properties, we build composites of the identified roll clouds (See~~Our measurement strategy across cloud streets allows us to detect the individual roll circulation objects (Sect. 3.2). For ~~this purpose, we group cloud properties according to their distance from the maximum updraft region~~

~~($Ze_{0.7}$).~~ the following statistical assessment, we use objects that have at least five successive radar measurements, i.e., 344 and 109 objects on 01 and 04 April, respectively, and refer to them as 'clouds'. First, we investigate the location of its updraft center ($Ze_{0.7}$ ~~within a cloud of the 'cloudstreet' regime (Fig. ??a). Generally, the roll circulations on 01 April evoke clouds that typically~~) within the cloud. As explained before, objects are not necessarily symmetric. However, most clouds form centered around the updraft of the circulation: ~~most frequently (46~~ around 50 % ~~)~~ of the time, maxima of $Ze_{0.7}$ occur ~~at cloud center~~ within the central tercile of the cloud and only rarely ~~close~~ within the tercile closest to the lateral cloud boundary (~~Fig. ??a~~ 7 %).

~~Cloud properties of cloud streets~~ To characterize how dynamics within roll circulations affect cloud and precipitation properties, these are composited for their relative distance to $Ze_{0.7}$ ~~in Fig.??c-o.~~ (Fig. 7). More precisely, we group cloud properties according to their distance from the maximum updraft region ($Ze_{0.7}$) into three regions: the central updraft region, the region close to cloud boundary, and the region in between.

On 01 April, the median of several parameters ~~has trends though their variability, as~~ shows consistent behavior although the variability, expressed by the interquartile distance, is high: CTH increases by ~~14~~9 % ~~(Fig. ??c) from~~ from the cloud boundary until the location of ~~maximum $Ze_{0.7}$. Consistent with cloud~~ the maximum updraft. In line with liquid formation within updrafts, LWP ~~(23~~ increases (22 % ~~; Fig. ??g)and the~~). The mean of Ze over each profile (~~81~~82 %) and S (42 % ~~; Fig. ??h) increase)~~ increase, undermining our assumption of the enhanced ice production in updrafts. In contrast, a decrease of LLT (~~29~~32 %; ~~??e)~~ by 20 m can be seen, which exceeds the ~~error in CTH~~ uncertainty of 10 m. ~~This could be explained by the transport of ice particles by the updraft~~ We hypothesize that updrafts transport ice particles into higher parts of the clouds~~, thus increasing the~~. The mixed-phase region thus increases at the expense of the liquid layer ~~.~~

~~The distribution of~~ and riming is enhanced (Fig. 4.2). Riming increases ice particle size, Ze, and S ~~widens inside the clouds because particularly large~~ in updrafts. The observed LWP increase in updrafts might indicate that condensation is more favored than depletion of liquid.

Strong riming events might explain the frequent high extremes of S ~~evolve more extreme, while the distributions of LLT and mean Ze become more narrow~~. Precipitation events do not only intensify at ~~the updraft location~~ updraft locations, but with 87 compared to ~~58~~55 % of the profiles, also more profiles contain precipitation than at cloud ~~boundaries (Fig. ??n)~~ boundary. On 01 April, we expect that most ice, indicated by $Ze_{\max}$, occurs at 0.6 of ~~D~~ the hydrometeor depth for updraft positions (Fig.~~??l). At the cloud boundaries, most ice crystals are located at~~ 7k). Large rimed particles close to cloud top might lift the height compared to the cloud boundary, where most ice is located within the lowest third of ~~D.~~ the hydrometeor depth.

On 04 April, ~~updrafts form least likely at the cloud boundary as well (23 %; Fig. ??b), however, less symmetrical around the center as on 01 April. Moreover, the~~ the absolute increase of CTH ~~increases in the updrafts by only 7% (Fig. ??d). The increase rate of S (Fig. ??k)~~ and mean Ze ~~(Fig. ??i)~~ within the clouds is about a factor of two lower than on 01 April. Moreover, S and LLT ~~stays~~ stay constant within the clouds~~(Fig. ??f). LWP is not investigated here because the low values on 04 April~~are ~~close to the detection limit of the measurements. At cloud boundary,~~. For all locations, the normalized height with most ice is similar to the one at cloud boundary on 01 April. The smaller MCAO strength seems to explicitly weaken the updraft motion and thus suppress the rise of CTH and the lifting of ice into the liquid layer in updrafts. In updrafts, this prevents riming, which hampers an increase in S and mean Ze, as well as the lifting of the height with most ice~~within the cloud is similar to 01~~

~~April, but it increases by only 37 % at updraft position (Fig. **??**m).~~ The precipitation fraction is lower <u>compared to 01 April</u>, i.e., only half at cloud boundary, but the increase ~~by 34 percentage points is similar to 01 April (Fig. **??**o).~~

~~The composites of the two cases show specific cloud property characteristics that can be used to evaluate high-resolution model simulation runs. Shupe et al. (2008) found conditions similar to the stronger case on 01 April with an increase of CTH and LWP at updrafts of Arctic MPCs during non-MCAO conditions over land. For this case, LWP reached much higher values of about 140 g m^{-2} for low LWP cases, and their layer thickness of pure and mixed liquid was about 300–500 m with larger values at updraft locations. For their time series, the thickness of the liquid-only layer decreased in the updraft similar to our findings. For MPCs over sea ice observed during SHEBA, the ice water content peaked in altitudes of 0.6 of the cloud depth (Shupe et al., 2006)~~<u>within the clouds is with 30 percentage points similar</u>.

4.4 Development along fetch

To investigate how the open water surface affects roll circulation and cloud properties, we analyze their ~~frequency of occurrence and~~ evolution over all observed fetches (Fig.~~8). We focus on roll circulation morphology first and use wavelength (λ) and aspect ratio (AR) as metrics (Sec. 3.2). Here, we only concentrate on the 'cloud street' regime where the roll circulation is well developed.~~

~~On 01 April, the vertical extend of the roll circulation as indicated by CTH is with a median of 700 m more than twice that high than on 04 April (300 m; Fig. 8a, b, I). On both days, CTH clearly increases with fetch. The growth rate is by a factor of more than two higher on 01 April, however, a stagnation at 100 km fetch can be observed on that day. On both days, the frequency of occurrence and median of λ (around 1.2 km) are similar (Fig. 8c, d, II). Generally, λ increases slightly with fetch on 01 April and reaches 2 km after 150 km approaching the width of the cloud streets seen by MODIS (2 km; Fig. 1). On 04 April, λ stays roughly constant and aligns with the cloud street width of the MODIS images (1 km; Sect. 4.1). Regarding mean values, λ is similar on both days, while CTH is roughly a factor of two larger on 01 April. Consequently, the median AR (Fig. 8III) is smaller on 01 April at 1.8 than on 04 April at 3.9. On both days, AR stays constant with fetch at large fetches, while it decreases at small fetches (Fig. 8e, f). This decrease is strengthened on 04 April by the unexpectedly high AR values that exceed 10. These values are provoked by weak convection at small fetches that are no roll circulations yet.~~

~~Development of geometrical and microphysical cloud properties with fetch on 01 April (first column) and 04 April (second column): cloud top height (CTH; a, b), wavelength of the circulation (λ; c, d), aspect ratio of the circulation (AR; e, f), horizontal cloud cover per minute (g, h) measured by the radar MiRAC (black) and lidar AMALi (blue), liquid layer thickness (LLT; i, j), liquid water path (LWP; k, l), mean radar reflectivity over each profile (mean Ze; m, n), snowfall rate at 150 m height for precipitating events only (S; o, p), precipitation fraction (q, r), and amount (s, t) of measured profiles (black) and identified cloud circulations (blue) per fetch bin. All AR above 10 are caused by large λ evoked by neighboring, cloud-forming convection that is not established as roll circulation yet. The red lines show the linear regression (a, b) and the course of the mean of the distribution for each fetch bin (c–f; i–p). The vertical gray lines (dashed) indicate the regime change from 'prior to cloud streets' to 'cloud streets' (Sect. 3.1). For robustness, bins of fetches with less than 10 roll circulation objects and of the 'prior to cloud street' regime are neglected to analyze the circulation (c–f; shaded). Boxplots (third column) show each~~

~~distribution's median and interquartile range within the 'cloud street' regime (I-VII). The total amount of measurements (N) is given for each parameter and day.~~

640 ~~Next, we investigate the cloud properties as a function of fetch. Cloud cover starts to strongly increase at small fetches as can be seen in radar (black) and lidar (blue) measurements~~ 8). The most prominent characteristic of an MCAO event is the rise in boundary layer height driven by the strong heat fluxes when air flows over the relatively warm ocean. Already in the MIZ the evaporation and convection lead to the appearance of first, still unorganized clouds in the 'prior to cloud street' regime, though horizontal cloud cover is low (Fig.~~8g, h). Here, horizontal cloud cover is defined as the ratio between the number of~~

645 ~~cloud-containing and all profiles temporally averaged over one minute. The increase is strongest at 10–20~~ 8g). Within the 'cloud street' regime, cloud cover increases quickly, and for fetches larger than 30 km~~fetch, and nearly complete cloud cover appears for larger fetches. The cloud cover from the radar is on average 4.5 % higher than that of the lidar, which might come from the radar's coarse horizontal resolution. The few cloud-free areas are small since 85 % of the observed cloud-free areas are less than 0.5,~~ cloud cover becomes higher than 90%. The comparison of boundary layer height BLH derived from dropsondes

650 and closely located airborne measurements showed that CTH is generally only by 8.5 ~~km wide~~ m lower than BLH, which suggests that we can use CTH as a proxy for BLH. CTH strongly increases with fetch (Fig.~~??a)~~ .

~~Further, we investigate how exposure to open water influences cloud microphysical parameters~~ 8a) and with distinct differences between 01 and 04 April. On 04 April, ~~90 % of the profiles containing liquid-topped cloud streets have LLT smaller than 100 m, which is more than on~~ the reduced buoyancy within ABL and warm air advection above BLH diminish the median CTH by

655 more than half compared to 01 April ~~(70 %) when thicknesses of up to 500~~to 300 m ~~are observed~~ (Fig.~~8i, j, IV). Consequently, median LLT is higher on 01 April (75 m) than on 04 April (50 m). No clear trend with fetch is evident.~~

~~The LWP distributions of cloud streets differ between both days (Fig. 8V) . On 01 April, the retrieved LWP quartiles range from around 40 to 60 g m^{-2}, the median is slightly below 50 g m^{-2}, and thus LWP is generally higher than on 04 April (interquartile range 0–25 g m^{-2}; median 12 g m^{-2}). Note that the maximum uncertainty in LWP is estimated to be 30 g~~8b)

660 and the growth rate of CTH with fetch by roughly 55 ~~m^{-2} (Sec. 2.2). On average, LWP increases with fetch~~ % (Fig.~~8k, l). On 01 April, LWP is more constant for fetches between 70 and 120 km and even decreases for fetches larger than 140 km. This decrease results in a 50 % smaller total increase of LWP over all observed fetches compared to 04 April, even though the absolute values are generally lower on 04 April.~~

~~On 01 April, the median of the mean radar reflectivity Ze over each cloudy cloud street profile is around -7 dBZ (Fig. 8VI).~~

665 ~~With around -12 dBZ, this value is lower on 04 April. Mean Ze increases with fetch mainly within the first 70 km on both days, whereby the distribution is more narrow on 04 April. Most interestingly is the more frequent occurrence of values above -5 dBZ on 01 April as they indicate snowfall.~~

~~For precipitating cloud street profiles, the upper quartile of S is slightly below 0.2 and around 0.1 mm h^{-1}~~ 8a). Note that this factor of roughly two is also evident in the BLH trend obtained from dropsondes (Table 2). The increase in CTH

670 with fetch is roughly linear, though on 01 ~~and 04 April, respectively, however, the lower quartile (0.75 mm h^{-1}) and median (0.1 mm h^{-1}) are similar on both days (Fig. 8VII) The course of S (Fig.8o, p) follows the one of Ze, as S is derived from it. With 0.07 mm h^{-1}km^{-1}, the increase rate is similar on both days. Differences between the days are a larger variability within~~

each fetch bin on 01 April and a shift of S by 10April, subsidence (cf. Fig. km towards larger fetches on 04 April. Hence, precipitation starts forming at fetches of 26 and 393) provokes a stagnation of CTH at around 100 km on 01 and 04 April, respectively.

fetch (2.5 h travel time). For fetches larger than 160140 km on 01 April, CTH, cloud cover, LWP, mean Ze, and precipitation fraction probably decrease and also other cloud parameters decrease, probably due to a remaining lee effect caused by Svalbard. Even though ERA5 reanalysis with its coarse resolution shows a rising air mass for cloud streets at these fetches (Fig. 8), we suggest that the air mass subsides and thus forms low, non-precipitating clouds with small particles. In summary, all analyzed microphysical properties differ between the MCAO events, particularly LWP and mean Ze.We observe slight changes in microphysical parameters with fetch.For most properties, the growth rates are similar on both days. However, the strength of the parameters is generally higher on 01 April when the $MCAO$ index is higher. The average S with fetch on 04 April lags behind the one on 01 April by 10 km. suppresses cloud development.

It has to be stressed, that the observed circulation and cloud evolution is not universal. As for our two cases, previous studies by Brümmer (1999), Murray-Watson et al. (2023), Gryschka et al. (2008) or Tornow et al. (2021) have shown that clouds in MCAOs are highly variable and depend on the initial conditions. Nevertheless, some of our findings align with other case studies. For low cloud cover over sea ice, Brümmer (1996) found an increase in CTH and cloud cover with fetch similar to our results . Our median λ values align with Next, we focus on the circulation characteristics, i.e., wavelength λ values obtained during the KonTur experiment (Brümmer et al., 1985; Markson, 1975; Brummer et al., 1982), ARKTIS '88 (Brümmer et al., 1992) , '91 and '93 (Brümmer, 1999), and MIZEX (Walter and Overland, 1984), i.e., 1.2 to 7 km at 250and aspect ratio, of the 'cloud street regime'. Note that bins in fetch with less than 10 roll circulation objects are not analyzed to avoid results being contaminated by outliers. Thus, data gaps around fetches of 50 km fetch.Similar to the 01 April, previous studies showed an increase of λ with fetch (Brümmer et al., 1992),e.g., Brümmer (1999) found a wavelength of 1.3 and 3.1 km near sea ice edge and 140exist (Fig. km downwind, respectively. Except for some outliers, particularly on 04 April , the AR of both days are similar to the observations during KonTur and MIZEX where a maximum of 4.6 was observed (Hein and Brown, 1988) .Hein and Brown (1988) derived the AR of the circulation from airborne gust probe measurement and also found that AR decreases with fetch from 3.3 at 1008c,e). Nevertheless, we can see some development with fetch: λ increases on 01 April (Fig. km downwind of the ice edge to 2.6 at 4508c) from roughly 1 to about 2 km . Other studies found both, decreaseing (Atkinson and Wu Zhang, 1996) and increasing AR with fetch (Brümmer, 1999; Brümmer et al., 1992). However, these observations did not focus explicitly on small fetches as we do.

Averaged over liquid MCAO clouds between 2008 and 2014, the evolution of cloud cover with fetch obtained by MODIS (Murray-Watson et al., 2023) is in line with our observations. With 91 % at 35 km fetch, MODIS obtained only a 4 % smaller cloud cover than averaged over both MCAOs of this study. However, their retrieved LWP of 60 g m^{-2} at sea ice edge and 130 g m^{-2} at 430a fetch of 150 km fetch is higher than during our cases. However, note that the satellite climatology explicitly excluded MPCs, which may explain the differences. The fact that MPCs are not studied explicitly by MODIS yet highlights the need for MPC observations.

5 ~~Impact of riming~~

~~Ice growth has implications on precipitation and thus on the lifecycle of MPCs (Korolev et al., 2017). Therefore, we investigate whether roll circulation influences riming within the cloud streets and whether riming evolves with fetch. In doing so, we use a subset of in situ and remote sensing data during which *P5* and *P6* were collocated (Sect.2). The data cover parts of the 'cloud street' regime only . To determine the degree of riming, we calculate the normalized rime mass (M) defined as the rime mass divided by the mass of the size-equivalent spherical graupel particle. Two methods following Maherndl et al. (2023b) are applied. The combined method uses the closure of in situ particle size distributions and Ze simulations obtained from running averages of in situ particle size distributions over 30~~ approaching the width of the cloud streets seen by MODIS (2 ~~s. The in situ method relates M to in situ particle shape measurements only. The results of both retrievals are comparable. However, since the collocation of *P5*~~ km; Sect. 4.1). Because the data used for the spectral analysis of riming are distributed over different fetches it seems likely that the peaks at 0.7 ~~and *P6* measurements might be inaccurate, we only analyze M of the in situ method for which no matching is necessary for the following. Note that our definition of updrafts might bias the following findings.~~

~~Normalized rime mass (M) obtained by the in situ method for collocated flight data of cloud streets on 01 and 04 April (a). The distribution of M is represented by a violin and box plot, where the horizontal line marks the median. The respective power spectrum of M on 01 April is shown in (b) with black lines marking important local maxima of the spectrum. Dependency of the normalized rime mass (M) obtained by the in situ method for cloud streets on 01 April on fetch (c) and updraft motion that is represented by $Ze_{0.7}$ (d). The red lines indicate the median of the M distribution for each fetch or $Ze_{0.7}$ bin.~~

~~Considering particles with a rime mass fraction above 10^{-2} as rimed, more rimed particles exist on 01 April (97~~ 1.1 km are linked to cloud streets (Fig. ~~%) than on~~ 6). On 04 ~~April (~~ April, the data only revealed reliable circulation information for fetches smaller than 80 km. For these fetches, λ stays roughly constant and aligns with the cloud street width of the MODIS images (1 ~~%). With a median M of $10^{-1.6}$ on 01 April~~ km; Sect. 4.1).

The data gaps also affect the analysis of ARs. In fact the large spread between the 5th and ~~$10^{-1.8}$~~ 95th percentile hints at the existence of some outlier. There is some evidence that AR decreases with fetch. For fetches larger than 60 km roll circulation is enhanced ~~on 04 April (Fig. 6a), riming is only significantly active in cloud streets on 01 April. In the following, the variability of M is investigated for 04 April. The spatial variability of riming is investigated by linearly detrended and mean-centered power spectra of M obtained during the seven collocated segments on~~ 01 ~~April (Sec. 2). Edge effects are minimized by applying a Hann window for smoothing. Note that M is not investigated at updraft locations obtained from remote sensing observations from P6 because the vertical motions differ for the in situ observations from P6. Due to the units of variance, the power spectrum increases automatically for smaller wavelengths. The average of the power spectrum of M peaks at about 0.7~~ April ~~and 1.1~~ a constant AR of about 2 is observed. This confirms the model by Brown (1972) stating that AR increases when less energy is available for convection. Regarding median values, λ is similar on both days (around 1.2 ~~km (Fig. 6b), thus, riming is variable at a spatial scale similar to the roll circulation (Fig. 8II). However, no general evolution of M is observed with fetch~~ km; Fig. 8d), while CTH is roughly a factor of two larger on 01 April ~~(Fig.6c). Instead, M increases with $Ze_{0.7}$~~

8b). Consequently, the median AR (Fig.6d) . We suggest that riming is enhanced in updraft regions 8f) is smaller on 01 April ,at 1.8 than on 04 April at 3.9.

5 Synthesis

The milestone of our study is the possibility of combining fine-resolved macro- and microphysical cloud observations in the initial MCAO transformation phase. In the following, we discuss the interaction between circulation, cloud macro-, and microphysical properties.Based on the two analyzed cases, the impact of the $MCAO$ index on these interactions is evaluated. The two scenarios and their different MCAO developments are illustrated by the schematic in Fig.9.This schematic summarizes the remote sensing and in situ measurements presented in Fig.3, 4, ??, 8, 6. Over sea ice, roll convection already forms, however, cloud streets have not developed yet. Prior to cloud street formation, the horizontal cloud extent and, with at most 10To investigate how the exposure to open water influences cloud microphysics, we look at the liquid layer thickness LLT (Fig. %, the horizontal cloud cover are small. The clouds have no separate liquid layer at cloud top. Mean Ze is relatively low, thus, the cloud particles are small and do not precipitate.

With fetch, the conditions develop: the averaged air temperature increases due to the presence of warm ocean water. This reduces the cooling rate of rising air masses and enhances the vertical extent of the largest turbulent eddies being ABL. For close locations, CTH is slightly smaller than BLH, which indicates that the ABL caps clouds. Hence, CTH increases with fetch. Roll circulations result in cloud streets after about 158h), LWP (Fig. km fetch that are mostly MPCs.

Sketch of the development of roll circulations and microphysics of the associated cloud streets with fetch on 01 April (first row) and 04 April (second row). The arrows at the bottom indicate the direction of the near-surface vertical motion.

The general evolution of cloud street properties within roll circulations is as follows: at the location of the strongest updraft, ice and liquid particles are lifted highest, which increases CTH, makes depositional growth of ice particles due to the colder temperatures more effective, and, thus, lifts the height with the highest ice mass within the hydrometeor depth. Due to larger ice particles over the whole cloud column, mean Ze and lowest maximum 8j), mean Ze increase, and the fraction of precipitation increases by roughly 30 percentage points . Due to the increased particle sizes, S averaged over all precipitation events, and particularly high (Fig. 8l) and S events increase. Descending or weak-rising motions next to the strongest updraft decrease the ice particle size and hence the averaged Ze. Note that high mean Ze might occur at boundaries of clouds with overall similar-strong updraft motions, where air descends mostly next to the cloud.

Within the 'cloud street' regime roll circulations and clouds are non-static but rather develop with fetch: at small fetches, some convection is not established as roll circulation yet, which increases λ. Due to large λ and relatively small CTH at small fetches, AR decreases logarithmically with fetch. For larger fetches and strong roll circulations, AR is constant (Fig. 8n). All parameters, with the exception of LLT, show a slight increase with fetch. This confirms the model by Brown (1972) stating that AR increases for little energy available from convection. The width of cloud streets increases with fetch leading to the strongest increase of cloud cover at 10–20. LWP is significantly higher on 01 April with a median of 50 km fetch, i.e., the initial cloud street formation, after which it is just below $100 gm^{-2}$ compared to 10 % gm^{-2} on 04 April. While the latter value

is below the absolute LWP error (see Sect. 2 observations for larger fetches exceed this value. The median LLT of 75 (50) m on 01 (04) April points at the dominant presence of liquid layer topped mixed-phase clouds in agreement with Table 2 showing 86% (71%) for the respective days. We attribute the constant LLT with fetch to the fact that both liquid (LWP) and ice (approximated by mean Ze) increase simultaneously, keeping the LLT constant.

~~While the evolution of thermodynamics, clouds, and roll circulations~~ The evolution of cloud microphysics with fetch is similar on both days, ~~different~~ however, thermodynamic conditions modify the intensity of the parameters. ~~Over sea ice, conditions are only slightly different: on 01 April, Ze values are a little lower likely due to drier conditions inside the ABL. CTH values are lower on~~ On 04 April ~~when dry air is advected above BLH.~~

~~Over water on 01 April, cloud top temperatures are colder than or at the low end of the temperatures within the dendritic-growth zone (DGZ; −20 to −10°C), where aggregation is a very dominant process (Chellini et al., 2022). This explains the high normalized rime mass. Contrarily to increasing $MCAO$ indices from rising SST, near-surface air mass subsides at 75 until 120~~, which features warmer temperatures, clouds are more shallow. On this day, 90 ~~km fetch on 01 April, which reduces the increase of CTH, mean Ze and LWP with fetch. Within the clouds,~~ % of the profiles containing liquid-topped cloud streets have LLT ~~decreases in updrafts because CTH from lidar and radar are about 60 and 80~~ smaller than 100 m ~~higher compared to cloud boundary, respectively. Due to their size and shape, ice particles might be lifted more strongly than liquid droplets and entrain parts of the pure liquid layer converting it into a mixed layer. Since the liquid is exposed to more ice particles, more liquid droplets might be depleted during riming. We expect this enhancement of riming in updrafts because M correlates with Ze. Riming increases ice particle size, Ze, and S in updrafts. The LWP increase in updrafts might indicate that condensation is more favored than depletion of liquid.~~

~~On 04 April, riming is not active because the cloud top temperatures lie within the DGZ where aggregation is favored. Within the clouds, less lifting indicated by lower $MCAO$ indices lowers the altitude of most ice with regard to hydrometeor depth particularly at the strongest updraft by half compared to~~, which is more than on 01 April ~~. Additionally, LLT stays constant because liquid and ice particles are lifted by the same amount. Ze and S increase in updrafts probably due to large dendrites that form by aggregation. The reduced buoyancy and warm air advection above BLH diminish the vertical extend of the ABL, and thus the growth rate of BLH and CTH with fetch by roughly 55~~ (70 %~~compared to 01 April. AR is higher on 04 April because smaller CTH are not compensated by λ, which on average stays constant. Particularly at small fetches, weak convection increases AR confirming Brown (1972). On 04 April, more shallow clouds exist with fewer parts of possible supercooled liquid and warmer supercooled liquid layer temperatures.~~). Less supercooled liquid reduces the amount of liquid-topped cloud profiles (Table 2), LWP (Fig. 8k) and LLT ~~. The~~ (Fig. 8i). The warmer temperature, low amount of supercooled liquid, and weak ~~convection~~ MCAO index prevent riming and reduce ~~S~~ snowfall rate and mean Ze ~~even with favored aggregation. All these mechanisms~~. This can explain why snowfall, occurs less frequently on 04 April. Moreover, missing riming in updrafts reduces the variability in snowfall rate within each fetch bin. No preconditioning by riming might delay the precipitation onset on 04 April by more than 10 km ~~.~~ (Fig. 8p). Hence, precipitation starts forming at fetches of 26 and 39 km on 01 and 04 April, respectively.

5 Conclusions

Our study investigates the evolution of thermodynamics, cloud/circulation morphology, cloud microphysics, and ~~riming for precipitation within~~ the first 170 km fetch ~~of two MCAO events. Previous studies resolved the initial phase of MCAO transformation, which determines the subsequent evolution, only coarsely and did not combine micro- with macrophysical cloud and circulation properties. We investigate high-resolved airborne remote sensing observations of two MCAOs observed during~~ (about 4 hours of travel time) during a long-lasting cold air outbreak in the Fram Strait. Airborne remote sensing and in situ observations were performed as part of the HALO-(AC)[3] campaign ~~in a quasi-Lagrangian way using back trajectories. We establish~~ within two research flights, just three days apart. A unique sampling strategy with research flights oriented perpendicular to cloud streets provided the opportunity to analyze fine-resolved macro- and microphysical cloud and circulation observations in the initial MCAO phase in a statistical sense. Specifically two metrics were developed for this purpose: The first one makes use of a ~~a~~ novel approach to detect roll circulations from vertical radar profiles only~~, allowing us to answer the posed research questions (Sec. 1).~~. This enables us to composite cloud and precipitation parameters as a function of their position within the roll circulation. The second metric uses back trajectories to analyze the cloud and circulation development with fetch, which allowed us to draw a consistent picture of the MCAO developments on 01 and 04 April 2022 (Fig. 9). Furthermore, the findings help to answer the research questions posed in Sect. 1:

I. ~~Which thermodynamic conditions characterize the two MCAO events?~~

~~The two events on 01 and 04 April~~ What are the differences between the environmental conditions on both flight days, and what are their implications on cloud development?

Both MCAO events feature northerly winds advecting dry and cold air masses into the Fram Strait. The event on 01 April shows colder air temperatures leading to a factor of two stronger *MCAO* MCAO index and stronger ~~surface fluxes. Wind shear induced by wind speed (~~heat fluxes. The more active convection on 01 April ~~) and wind direction (~~compared to 04 April ~~) is present.~~

II. ~~Which cloud properties are associated with roll circulation?~~

~~A composite analysis reveals that, compared to cloud boundary, updrafts increase~~ deepens the boundary layer, causing higher cloud top heights that are well aligned with the boundary layer height. A rough scaling with a factor of two can be assumed for all parameters between both days. One also has to note that the island of Svalbard influences the flow. This provoked a wave effect in the lee of Svalbard on 01 April with subsiding air masses and thus reduced cloud top heights ~~, liquid water path, snowfall rate, and the height within the cloud containing most ice.~~ at 75 to 100 km fetch. On 04 April, lee effects caused an even stronger cloud-free zone west of the island, which led to a convergence zone and was not considered in the analysis.

The difference in cloud top height between lidar and radar is used to diagnose the liquid layer thickness LLT, which indicates the presence of supercooled-liquid layer topped mixed-phase clouds for 86% (71%) of the time on 01 (04) April. With respect to cloud microphysics, the most prominent difference between both days is that riming is only significantly active during the cold and strong MCAO case on 01 April. This day also features a higher amount of supercooled liquid

water with median liquid water paths of roughly $50\,\mathrm{g\,m^{-2}}$. Riming influences LLT, radar reflectivities, precipitation onset, and strength by producing larger ice particles. Regarding median properties, cloud ~~top height,~~ liquid layer thickness, liquid water path, and snowfall rate are again roughly a factor of two lower for the weaker MCAO on 04 April.

III. Can we identify characteristic changes in cloud and precipitation properties perpendicular to cloud street orientation, i.e., within the roll circulation?

Yes, several hundred roll circulation objects were identified using cloud radar measurements performed on multiple legs perpendicular to cloud street orientation. A composite analysis of these objects reveals that on 01 April, several parameters show consistent trends from the updraft region towards cloud boundaries, while on 04 April, only increased radar reflectivity and precipitation can be found in the updraft region. We hypothesize that the presence of significant riming on 01 April leads to increases in liquid water path, snowfall rate, and the height towards the updraft center while the LLT decreases because updrafts lift ice particles into the pure liquid layer. Our statistical analysis of mean cloud characteristics within the roll circulation and their variability could be used to test the performance of cloud parameterizations and better understand riming effects.

IV. How do ~~circulation and cloudproperties change~~ roll circulation, cloud, and precipitation properties evolve with fetch in the initial ~~state of MCAOs and when do cloud streets start to precipitate?~~
~~An increase with fetch is found for boundary layer and~~ MCAO phase, e.g., up to travel times of 4 hours?
Analyzing our measurements as a function of fetch shows increasing cloud top height, ~~temperature and humidity of the boundary layer,~~ liquid water path, radar reflectivity, near-surface precipitation rate, horizontal cloud cover, and ~~the~~ fraction of precipitating profiles. Cloud streets form at around 15 km fetch and start precipitating at 25 to 40 km. The later onset of precipitation on 04 April is attributed to the lack of riming. The aspect ratio of the roll circulation decreases with fetch for ~~small fetches~~ fetches smaller 50 km and stays constant for larger fetches. The ~~studied cloud streets start precipitating at 25–30 km.~~

V. ~~What is the impact of riming on MCAO transformation?~~
~~For riming to be active, it has to be colder than -20°C. On~~ wavelength of the cloud streets λ slightly increases with fetch on 01 April ~~, maxima in the normalized rime mass have a horizontal spatial scale similar to the roll circulation but do not depend on fetch~~ but the variability is rather high. Nevertheless, λ is just barely larger than 1 km within the first 100 km as also found in the spectral analysis of riming. Such small scales are extremely difficult to resolve from space, highlighting the importance of airborne measurements.

~~We~~ To answer the two last research questions, we established composite approaches to characterize the roll circulation ~~and fetch dependence~~ (Fig. 7) and fetch (Fig. ~~?? and~~ 8). Such metrics can also be generated from ~~high-resolution~~ cloud-resolving model output and be used to evaluate their performance to represent microphysics and dynamics in the initial phase of an MCAO. By considering the two cases with similar large-scale synoptic settings but differences with respect to microphysics, e.g., LWP and riming, insights into the simulation of cloud microphysics could be gained. In particular, it will be interesting to analyze whether such models successfully reproduce the ~~difference between both cases and whether the~~ observed factor of two ~~scaling appears.~~ in scaling found for several parameters between the two cases.

~~It would have been interesting to characterize the impact of the marginal sea ice zone (MIZ) on the air mass transformation. However, too few data with variable fetches due to different fetches over MIZ only exist.~~ To study the impact of the sharpness of MIZ and flow divergence on cloud evolution, more observations at constant fetches over open water and variable fetches over MIZ near the sea ice edge must be obtained in the future. Moreover, since the observed cloud top temperatures lie within the dendritic-growth zone, aggregation would be another interesting process to study, which is possible by dual frequency radar observations (Chellini et al., 2022).

The Clouds over cOMPlEX environment (~~COMPlEX) campaign~~ COMPEX) campaign planned for spring 2026 northwest of Svalbard will raise the opportunity to ~~study clouds near sea ice edge where an airborne W- and~~ better characterize the impact of the marginal sea ice zone (MIZ) on the air mass transformation. Flights within the MIZ and along the ice edge could increase the number of samples. Further, by enhancing our measurement suite with an airborne G-band radar~~will be operated northwest of Svalbard in spring 2025.~~, more information on cloud microphysics can be deduced.

Appendix A: ~~Error of fetch induced by resolution limitations~~ Peak detection algorithm and sensivity

~~The temporal resolution of the calculated fetch is 1~~ To detect up- and downdrafts, we solely use $Ze_{0.7}$, which are radar reflectivity measurements at the height of 0.7 of the hydrometeor depth (D; Sec. 2.2). Figure A1 explains the choice of this height (red line). To understand the applied height and Ze thresholds, one has to keep in mind that Ze values larger -5 ~~min. We calculate back trajectories from ERA5 wind fields with a horizontal resolution of roughly 30~~dBZ (Schirmacher et al., 2023) ~~and below 500~~ ~~km. For an average flight speed of 80~~m (Shupe et al., 2008) height are defined as precipitation. At 0.7 of the hydrometeor depth, most largest cloud particles occur, i.e., most maximum Ze per profile exceeding -10 ~~m~~dBZ taken among all non-precipitating values (Fig. ~~s^{-1}, *P5* travels a~~distance of about 5~~A1a, gray line). Most maximum Ze per profile among non-precipitating radar bins occur at cloud bottom (Fig. ~~km during one minute. Taking the same trajectory for all measurements within one minute thus does not reduce the spatial resolution.For SIC~~A1a, black line). Nevertheless, this bottom-near maximum is induced by very small Ze values below -10 dBZ. Since we aim to detect updrafts at the selected height, we take the height where large particles (>-10 dBZ) occur most frequently. Moreover, with 98 %, most precipitation occurs below 0.7

of the hydrometeor depth (Fig. A1b, dashed black line). This finding is not sensitive to the -5 dBZ threshold for precipitation (Fig. A1b, dashed gray line). Dry entrainment and liquid droplets seem rare at 0.7 of the hydrometeor depth since 91 % of the lowest Ze per profile lie above this altitude (Fig. A1b, solid black line). In conclusion, we take ~~merged MODIS-AMSR2 data with a horizontal resolution of 1~~Ze at the height of 0.7 of the hydrometeor depth to consider the largest ice particles within the profiles and minimize the influence of dry air entrainment/supercooled liquid water droplets at cloud top and precipitation at the bottom of the hydrometeor depth.

To find up- and downdraft regions using $Ze_{0.7}$, we follow this recipe:

   I. Determine 0.7 of D for every profile (Fig. ~~km (Ludwig et al., 2020). The ERA5 wind field is relatively homogeneous.Thus, neighboring trajectories do not differ significantly (Fig. 1e, f). Differences in fetches between two neighboring trajectories mainly come from differences in SIC along the trajectories.The median of the relative change between two adjacent fetches is 9.6~~2b).

   II. Average Ze over 100 ~~%.~~ m in the vertical to reduce noise.

   III. Smooth Ze by averaging over 3 s to minimize noise detection (Fig. 2c).

   IV. Extract the smoothed $Ze_{0.7}$ at 0.7 of D for each profile, which is the average between 0.65 and 0.75 times D (Fig. 2d, black line).

   V. Derive the large-scale background Ze_{back} by averaging $Ze_{0.7}$ over 500 s ($\sim$ 40 km; Fig. 2d, gray line).

   VI. Determine peaks in $Ze_{0.7}$ using the python package scipy.signal.find_peaks (Virtanen et al., 2020).
If $Ze_{\mathrm{back}} \geq 0.67\,\mathrm{mm^6\,m^{-3}}$, find peaks for $Ze_{0.7}$ with a prominence of at least $0.5\,\mathrm{mm^6\,m^{-3}}$ (difference between the height of the peak and its lowest contour line; Fig. 2d, vertical orange line) and a width of at least 2.9 samples (about 230 m horizontal distance; Fig. 2d, horizontal orange line). Note that Fig. 2 shows Ze in logarithmic space while peaks are detected in linear space.
If $Ze_{\mathrm{back}} < 0.67\,\mathrm{mm^6\,m^{-3}}$, find peaks for $Ze_{0.7}$ with a prominence of at least $0.1\,\mathrm{mm^6\,m^{-3}}$ and a width of at least 2.9 samples.
The detected peaks are defined as updrafts (Fig. 2e, vertical black lines) Here, we apply two different thresholds depending on Ze_{back} since the magnitude of the averaged Ze and its peaks generally increase with fetch.

   VII. Find the minimum $Ze_{0.7}$ between every two maxima (Fig. 2e, vertical gray line). If conditions between two cloud streets are cloud-free, we consider the downdraft location at the center of the cloud-free distance.

Table A1. Sensitivity of the steps of the algorithm applied to identify roll circulation objects. Relative changes of the number of objects in total, number of objects inside the 'cloud street' regime, cloud top height (CTH) of cloud streets, and aspect ratio (AR) of the roll circulation to the results obtained by the applied configuration after adjusting, i.e., mostly doubling, parameters.

modification	total number of objects	number of objects within 'cloud street' regime	CTH	AR
III: average over 6 s	-17.8 %	-20 %	+24 %	+23 %
IV: 0.6 of hydrometeor depth	-1.8 %	-1 %	0 %	0 %
IV: 0.8 of hydrometeor depth	+3.4 %	0 %	0 %	0 %
VI: width of 5.8 samples	-31.3 %	-37 %	+59 %	+57 %
VI: If $Ze_{\mathrm{back}} \geq 0.67\,\mathrm{mm}^6\,\mathrm{m}^{-3}$: prominence of at least $0.2\,\mathrm{mm}^6\,\mathrm{m}^{-3}$	-9.8 %	-11 %	+10 %	+11 %
VI: If $Ze_{\mathrm{back}} < 0.67\,\mathrm{mm}^6\,\mathrm{m}^{-3}$: prominence of at least $1\,\mathrm{mm}^6\,\mathrm{m}^{-3}$	-9.3 %	-10 %	+10 %	+11 %
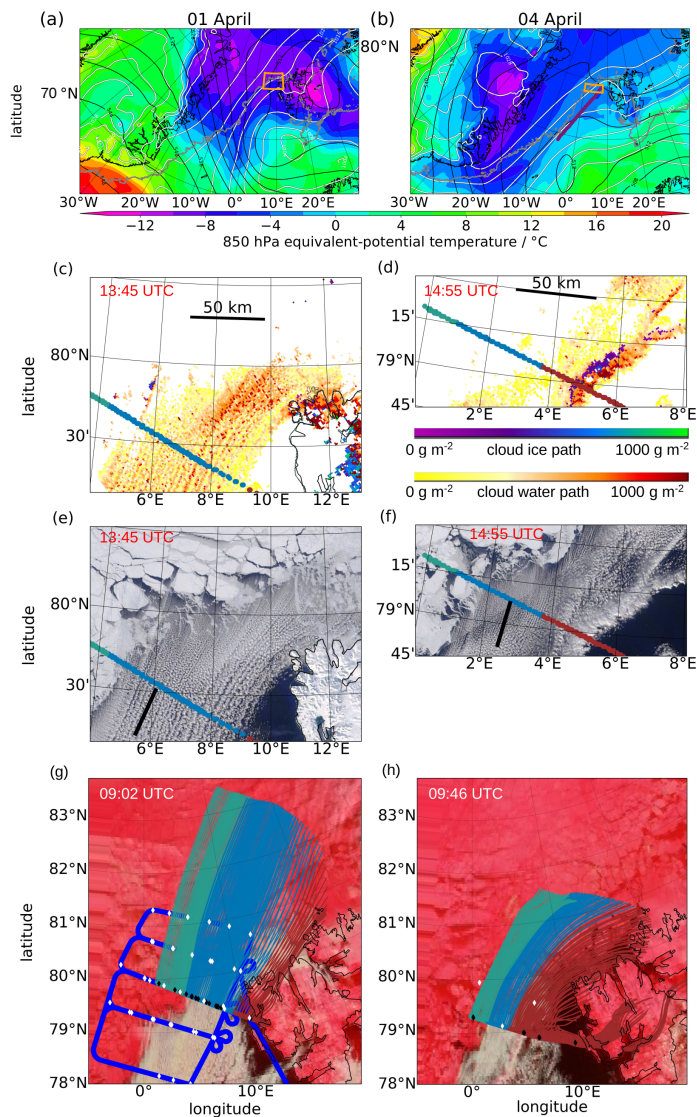
Figure 1. ~~Cloud situation on~~ Overview of 01 ~~April 2022~~ (left~~column~~) and 04 April 2022 (right~~column~~). ~~Observations~~ (a, b) Maps of ~~cloud water~~ mean sea level pressure (white contours), 500 hPa geopotential height (black contours), and 850 hPa equivalent-potential temperature (shading) from ERA5 at 12:00 UTC with 15 % sea ice concentration (gray dots), the flight area (orange) shown in c-h, and the convergence line (purple) on 04 April. (c,d) Total cloud water path (Nasa Worldview, 2023a; ~~a, b;~~ 1 km resolution) and (e,f) corrected reflectance (Nasa Worldview, 2023b; ~~c, d;~~ 500 m resolution) of ~~the Moderate Resolution Imaging Spectroradiometer~~ (MODIS ~~) on~~ Terra on 01 April (13:45 UTC) and 04 April (14:15 UTC). ~~The black lines in (c) and~~ Thick colored dots show P5 track, categorized by the measurement regime (~~d~~Table 1). Black lines represent the orientation of the cloud streets. ~~To better differentiate between sea ice and clouds, the corrected reflectance observed by the Visible Infrared Imaging Radiometer Suite (VIIRS) instrument aboard the joint NASA/NOAA Suomi National Polar-orbiting Partnership~~ (Nasa Worldview, 2023c; ~~eg,f~~h) ~~at 09:02 UTC on 01 April and 09:46 UTC on 04 April is shown. Additionally,~~ 12-hour near-surface back trajectories for the P5 measurement locations (~~thin~~ colored lines), dropsonde locations (diamonds) of P5 (black) and HALO (white), and the flight path of HALO on 01 April 2022 (blue line)~~are shown. The flight path of P5~~ Background image from Visible Infrared Imaging Radiometer Suite (~~thick colored line~~VIIRS) ~~overlays all maps. Here, the colors categorize the measurement regimes~~ (~~Sect. 3.1, Table 1~~Nasa Worldview, 2023c) at 09:02 UTC on 01 April and 09:46 UTC on 04 April.
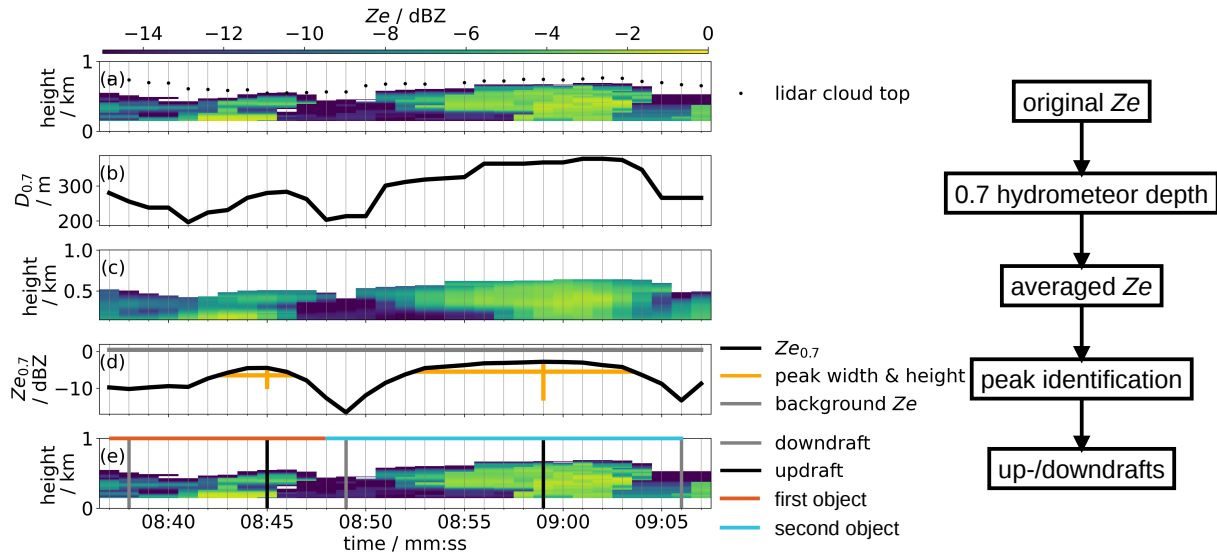
Figure 2. Visualization of roll cloud circulation identification. Time series (30 s) of the equivalent radar reflectivity Ze profiles measured by MiRAC starting at 10:08:37 UTC on 01 April (a), 0.7 of hydrometeor depth ($D_{0.7}$, b), Ze smoothed in space and time (c), smoothed Ze at $D_{0.7}$ (d, black) with its peak width and height (d, orange) and the background Ze (d, gray). The original Ze observations (same as in a), detected up- (black) and downdrafts (gray), and circulation objects (blue, red) are shown in (e). For comparison, the cloud top height observed by the lidar AMALi is displayed (a, black dots). The shown time period covers fetches from 73 to 80 km and corresponds to a flight distance of 7 km.
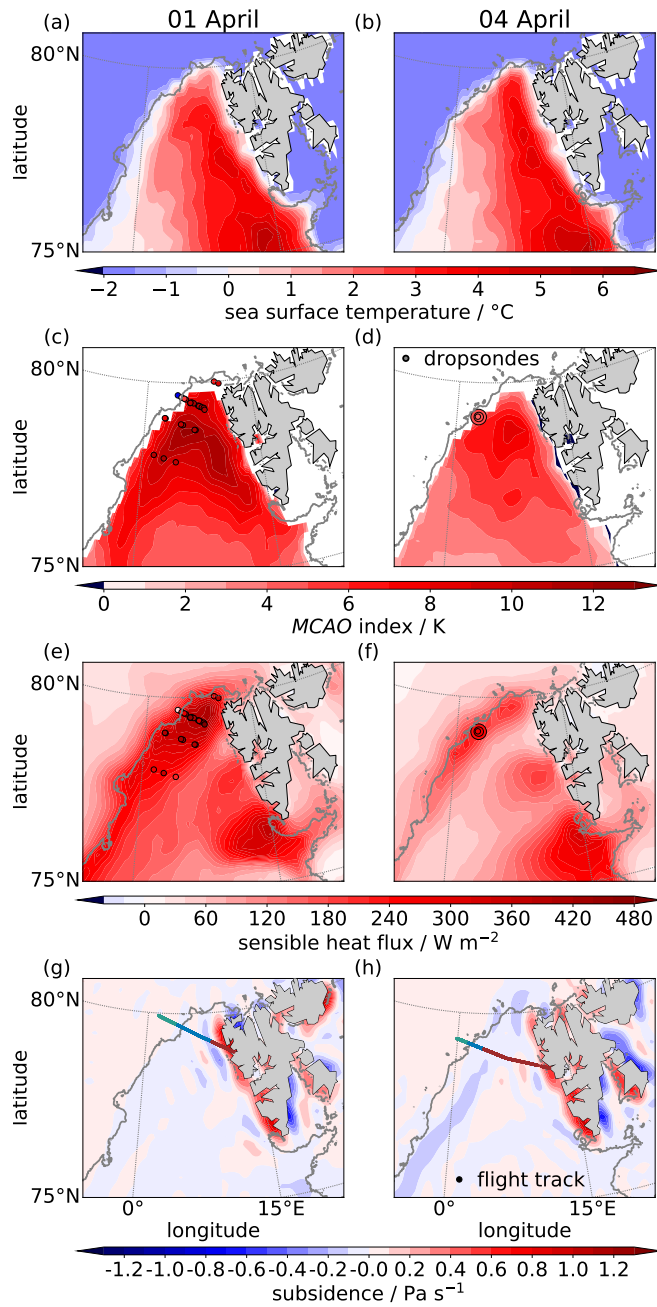
Figure 3. ~~Evolution~~ Overview of ~~*MCAO* index~~ environmental conditions on 01 April (~~first row~~left) and ~~subsidence at 1000 hPa~~ 04 April (~~second row~~right)~~with fetch on 01 April~~. Maps of MCAO index (a, b), sea surface temperature (c, d), and ~~04 April~~ subsidence at 1000 hPa (~~b, d~~e, f) from ERA5 reanalysis data. Positive subsidence values indicate downward motion. ~~The colors categorize the measurement regimes~~ MCAO indices from dropsonde observations are shown as circles (~~Sect. 3~~a, ~~Table 1~~b). ~~The triangles~~ Flight tracks in (~~a~~e) and (~~b~~f) ~~show the MCAO index retrieved from dropsonde measurements of~~ are color-coded according to the ~~research aircraft *P5* (red) and *HALO*~~ measurement categorization (~~orange~~Table 1). The gray lines indicate the 15 % sea ice concentration from ERA5.
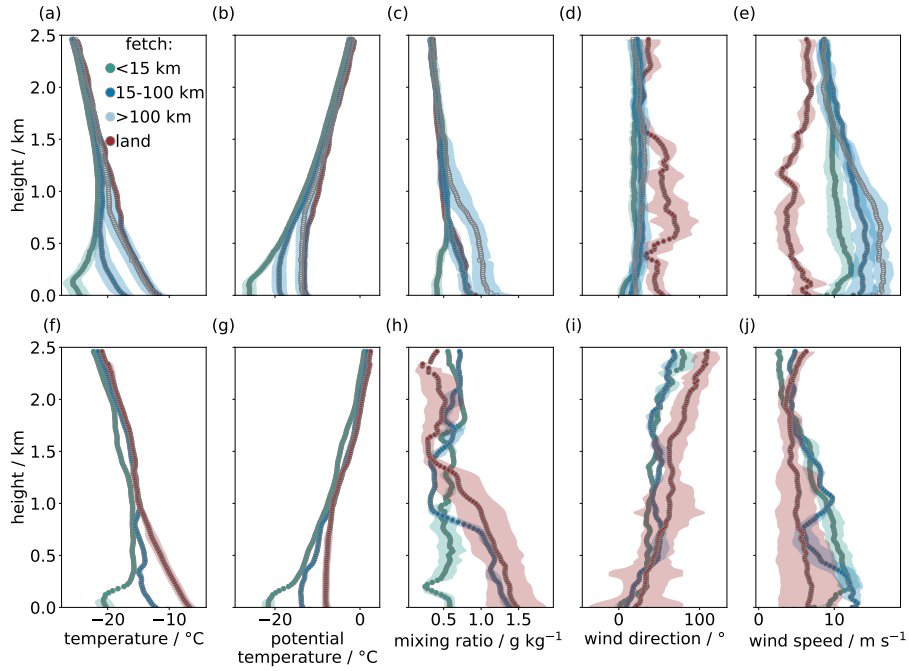
Figure 4. Averaged dropsonde profiles from *HALO* and *P5* of temperature (a, f), potential temperature (b, g), mixing ratio (c, h), wind direction (d, i) and speed (e, j) binned by fetch on 01 April (first row) and 04 April 2022 (second row). The shaded areas represent the standard deviation of each category. The color coding follows the categorization shown in Table 1. On 01 April, the number of dropsondes per category is 27 (<15 km fetch; green), 14 (15-100 km and >100 km fetch; dark and light blue), and 3 (land; red). On 04 April, the number is 3, 4, and 9, respectively.
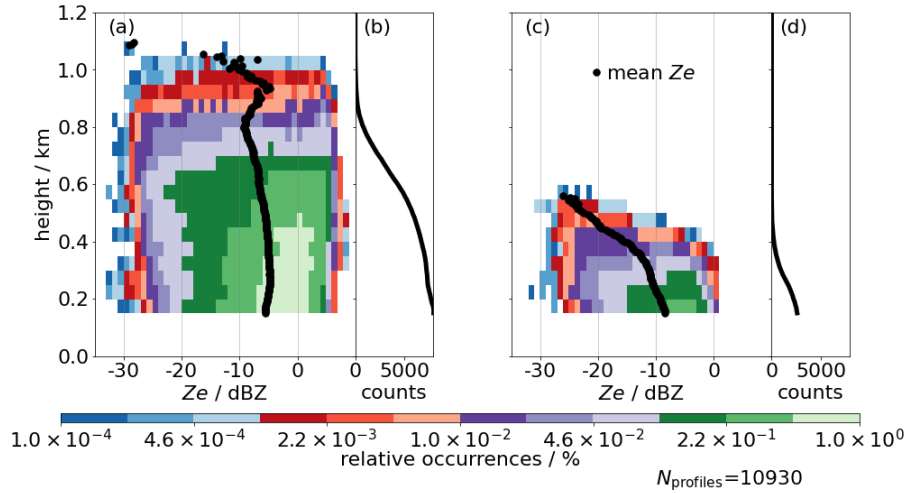
Figure 5. Contoured frequency by altitude diagram (a, c) and absolute counts per altitude (b, d) for all radar reflectivities (Ze) obtained by MiRAC in the 'cloud street' regime on 01 April (a, b) and 04 April (c, d). Moreover, each averaged Ze profile (black dots), and the total number of profiles (N_{profiles}) is displayed.
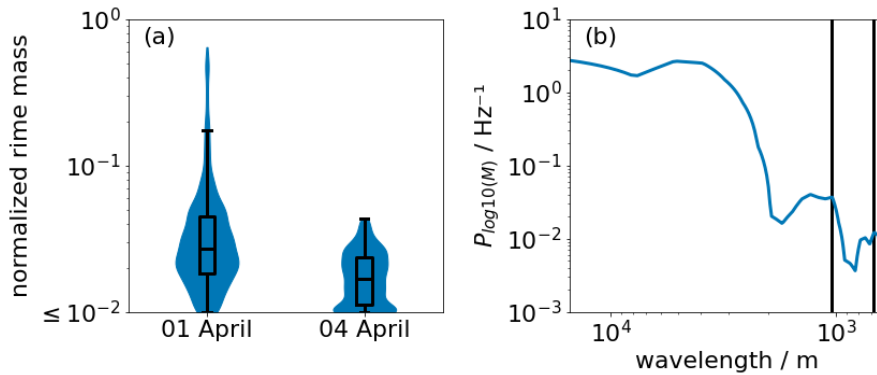
Figure 6. Left: Violin and box plot of the normalized rime mass (M) obtained by the in situ method for collocated flight data of cloud streets on 01 and 04 April. Right: Corresponding power spectrum of M on 01 April with black lines marking important local maxima of the spectrum.
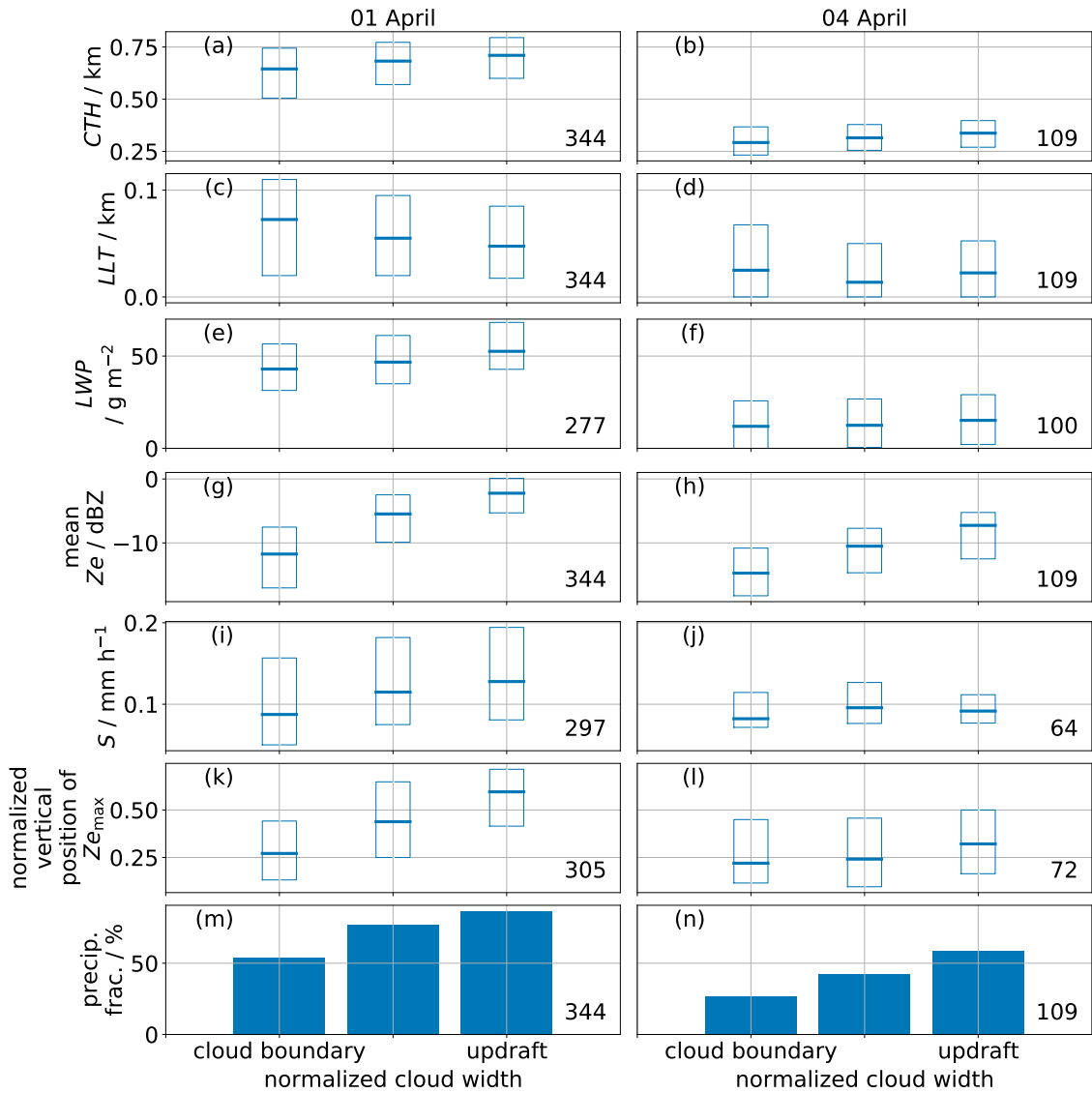
Figure 7. ~~Relative occurrence of updrafts (max $Ze_{0.7}$) within all cloud streets that consist of at least 5 radar profiles on 01 April (a) and 04 April (b).~~ Average composites of ~~their microphysical~~ cloud <u>and precipitation</u> properties within the normalized distance between lateral cloud boundary and updraft <u>(max $Ze_{0.7}$) for circulation objects within the cloud street regime</u> on 01 April (left column) and 04 April (right column): cloud top height (CTH; ~~e~~<u>a</u>, ~~d~~<u>b</u>), supercooled liquid layer thickness (LLT; ~~e~~<u>c</u>, ~~f~~<u>d</u>), liquid water path (LWP; ~~g~~<u>e</u>), mean radar reflectivity (Ze) over each profile (~~h~~<u>f</u>, ~~i~~<u>g</u>), snowfall rate at 150 m (S; ~~j~~<u>h</u>, ~~k~~<u>i</u>), vertical position ~~normalized by the hydrometeor depth~~ of the maximum Ze for each profile <u>normalized by the hydrometeor depth</u> (~~l~~<u>j</u>, ~~m~~<u>k</u>), and fraction of precipitating profiles (precip. frac.; ~~n~~<u>l</u>, ~~o~~<u>m</u>). The median (horizontal line) and lower and upper quartile (box edges) are displayed at the boundary of the clouds, the updraft position, and in between. <u>The total number of objects is given for every parameter separately.</u>

36
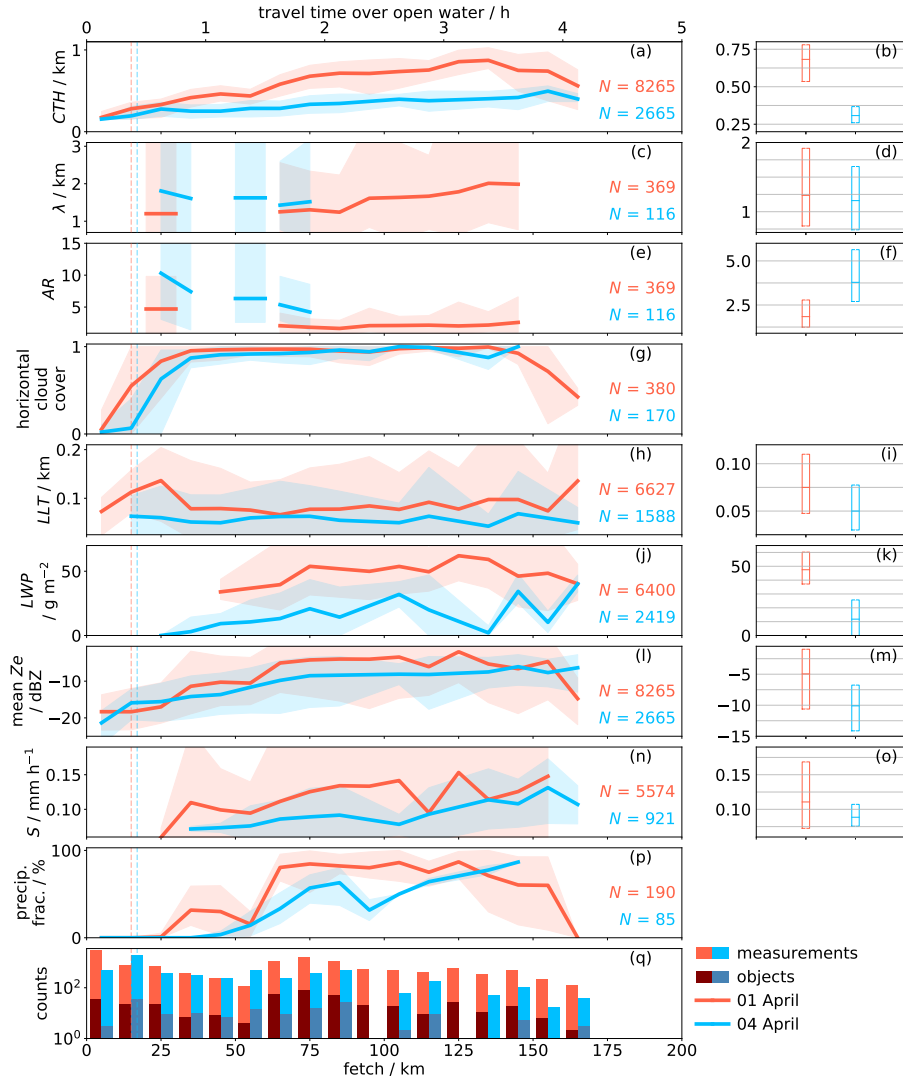
Figure 8. Left: Development of circulation, cloud, and precipitation characteristics with fetch on 01 (red) and 04 April (blue): cloud top height (CTH; a, b), wavelength of the circulation (λ; c, d), aspect ratio of the circulation (AR; e, f), horizontal cloud cover (g), liquid layer thickness (LLT; h, i), liquid water path (LWP; j, k), mean radar reflectivity over each profile (mean Ze; i, m), snowfall rate at 150 m height (S; n, o), precipitation fraction (p), and amount (q) of measured profiles (colored) and identified cloud circulations (gray) per fetch bin. LLT, LWP, and S statistics are only calculated when cloud/precipitation occurs. Lines and shades represent mean values and the 5th and 95th percentile, respectively. The vertical dashed lines indicate the regime change from 'prior to cloud streets' to 'cloud streets' (Sect. 3.1). Right: Boxplots show each distribution's median and interquartile range within the 'cloud street' regime. The total amount of measurements (N) is given for each parameter and day.
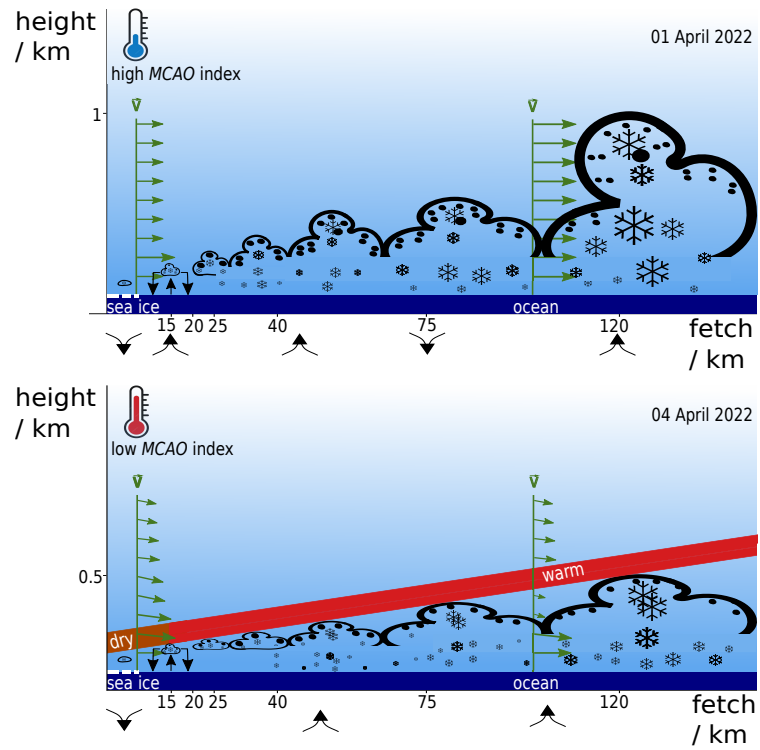
Figure 9. Sketch of the development of roll circulations and microphysics of the associated cloud streets with fetch on 01 April (first row) and 04 April (second row). The arrows at the bottom indicate the direction of the near-surface vertical motion.
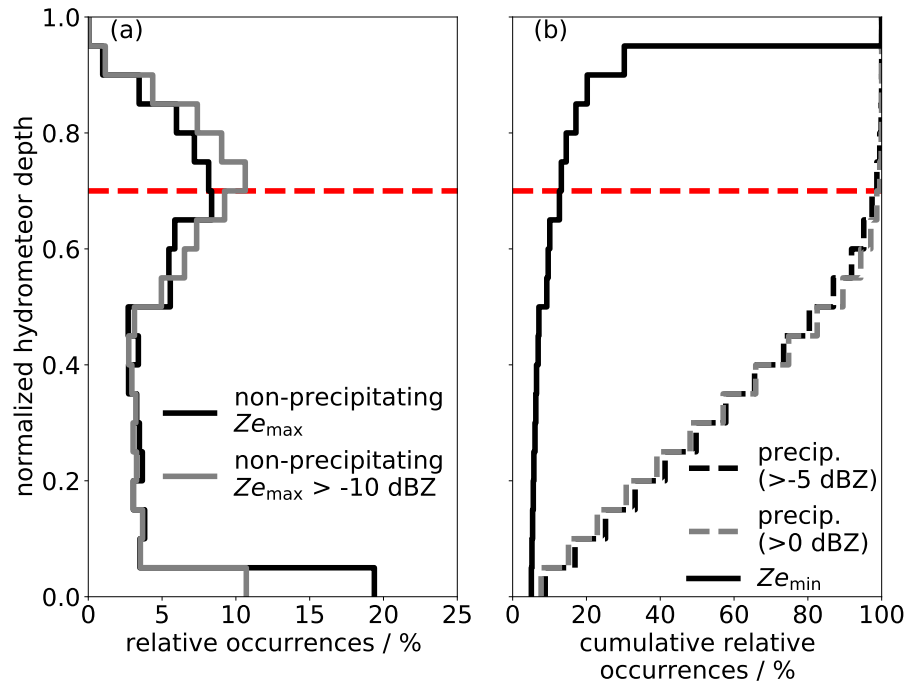
Figure A1. Relative occurrences of Ze_{max} among non-precipitating hydrometeors (a, black solid) and of non-precipitating Ze_{max} that exceed -10 dBZ (a, gray solid). Relative occurrence of precipitation defined by Ze values larger -5 dBZ (b, black dashed) and larger 0 dBZ (b, gray dashed), and minimum Ze of each radar profile (b, black solid). The y-axis is the normalized hydrometeor depth (0=base, 1=top). The height that is used to identify roll circulations is indicated by the red line.

Contoured frequency by altitude diagram (left) and absolute counts per altitude (right) for liquid-topped (first row) and non-liquid-topped (second row) radar reflectivity (Ze) profiles obtained by MiRAC in the 'cloud street' regime on 01 April (a, b, e, f) and 04 April (c, d, g, h). Moreover, each mean Ze profile (black dots) is displayed. The total amount of liquid-topped and non-liquid-topped profiles is 8979 and 1951, respectively.

940 Boxplots for cloud free distances (a) and the maximum radar reflectivity of each profile for the 'cloud street' regime on 01 April (left) and 04 April (right). The boxes show the median and interquartile rannge, and N the number of samples.

References

Abel, S. J., Boutle, I. A., Waite, K., Fox, S., Brown, P. R. A., Cotton, R., Lloyd, G., Choularton, T. W., and Bower, K. N.: The Role of Precipitation in Controlling the Transition from Stratocumulus to Cumulus Clouds in a Northern Hemisphere Cold-Air Outbreak, Journal of the Atmospheric Sciences, 74, 2293–2314, https://doi.org/10.1175/JAS-D-16-0362.1, 2017.

Ansmann, A., Tesche, M., Althausen, D., Müller, D., Seifert, P., Freudenthaler, V., Heese, B., Wiegner, M., Pisani, G., Knippertz, P., and Dubovik, O.: Influence of Saharan dust on cloud glaciation in southern Morocco during the Saharan Mineral Dust Experiment, Journal of Geophysical Research: Atmospheres, 113, https://doi.org/10.1029/2007JD008785, 2008.

Atkinson, B. W. and Wu Zhang, J.: Mesoscale shallow convection in the atmosphere, Reviews of Geophysics, 34, 403–431, https://doi.org/10.1029/96RG02623, 1996.

Baumgardner, D., Brenguier, J. L., Bucholtz, A., Coe, H., DeMott, P., Garrett, T. J., Gayet, J. F., Hermann, M., Heymsfield, A., Korolev, A., Krämer, M., Petzold, A., Strapp, W., Pilewskie, P., Taylor, J., Twohy, C., Wendisch, M., Bachalo, W., and Chuang, P.: Airborne instruments to measure atmospheric aerosol particles, clouds and radiation: A cook's tour of mature and emerging technology, Atmospheric Research, 102, 10–29, https://doi.org/10.1016/j.atmosres.2011.06.021, 2011.

Brown, R. A.: On the Inflection Point Instability of a Stratified Ekman Boundary Layer, Journal of the Atmospheric Sciences, 29, 850–859, https://doi.org/10.1175/1520-0469(1972)029<0850:OTIPIO>2.0.CO;2, 1972.

Brummer, B., Schlunzen, H., and Bogel, W.: Cloud streets duringKontur, pp. 63–77, 1982.

Brümmer, B.: Boundary-layer modification in wintertime cold-air outbreaks from the Arctic sea ice, Boundary-Layer Meteorology, 80, 109–125, https://doi.org/10.1007/BF00119014, 1996.

Brümmer, B.: Roll and Cell Convection in Wintertime Arctic Cold-Air Outbreaks, Journal of the Atmospheric Sciences, 56, 2613–2636, https://doi.org/10.1175/1520-0469(1999)056<2613:RACCIW>2.0.CO;2, 1999.

Brümmer, B., Bakan, S., and Hinzpeter, H.: Kontur: Observations of cloud streets and open cellular structures, Dynamics of Atmospheres and Oceans, 9, 281–296, https://doi.org/10.1016/0377-0265(85)90024-7, 1985.

Brümmer, B., Rump, B., and Kruspe, G.: A cold air outbreak near Spitsbergen in springtime — Boundary-layer modification and cloud development, Boundary-Layer Meteorology, 61, 13–46, https://doi.org/10.1007/BF02033993, 1992.

Chellini, G., Gierens, R., and Kneifel, S.: Ice Aggregation in Low-Level Mixed-Phase Clouds at a High Arctic Site: Enhanced by Dendritic Growth and Absent Close to the Melting Level, Journal of Geophysical Research: Atmospheres, 127, https://doi.org/10.1029/2022JD036860, 2022.

Copernicus Marine Service: Arctic Ocean - Sea and Ice Surface Temperature, https://doi.org/10.48670/moi-00130, (last access: 31 October 2023) [data], 2023.

Dahlke, S., Solbès, A., and Maturilli, M.: Cold Air Outbreaks in Fram Strait: Climatology, Trends, and Observations During an Extreme Season in 2020, Journal of Geophysical Research: Atmospheres, 127, e2021JD035 741, https://doi.org/10.1029/2021JD035741, 2022.

de Roode, S. R., Frederikse, T., Siebesma, A. P., Ackerman, A. S., Chylik, J., Field, P. R., Fricke, J., Gryschka, M., Hill, A., Honnert, R., Krueger, S. K., Lac, C., Lesage, A. T., and Tomassini, L.: Turbulent Transport in the Gray Zone: A Large Eddy Model Intercomparison Study of the CONSTRAIN Cold Air Outbreak Case, Journal of Advances in Modeling Earth Systems, 11, 597–623, https://doi.org/10.1029/2018MS001443, 2019.

Duscha, C., Barrell, C., Renfrew, I. A., Brooks, I. M., Sodemann, H., and Reuder, J.: A Ship-Based Characterization of Coherent Boundary-Layer Structures Over the Lifecycle of a Marine Cold-Air Outbreak, Boundary-Layer Meteorology, 183, 355–380, https://doi.org/10.1007/s10546-022-00692-y, 2022.

Ehrlich, A., Crewell, S., Herber, A., Klingebiel, M., Lüpkes, C., Mech, M., Becker, S., Borrmann, S., Bozem, H., Buschmann, M., Clemen, H.-C., De La Torre Castro, E., Dorff, H., Dupuy, R., Eppers, O., Ewald, F., George, G., Giez, A., Grawe, S., Gourbeyre, C., Hartmann, J., Jäkel, E., Joppe, P., Jourdan, O., Jurányi, Z., Kirbus, B., Lucke, J., Luebke, A. E., Maahn, M., Maherndl, N., Mallaun, C., Mayer, J., Mertes, S., Mioche, G., Moser, M., Müller, H., Pörtge, V., Risse, N., Roberts, G., Rosenburg, S., Röttenbacher, J., Schäfer, M., Schaefer, J., Schäfler, A., Schirmacher, I., Schneider, J., Schnitt, S., Stratmann, F., Tatzelt, C., Voigt, C., Walbröl, A., Weber, A., Wetzel, B., Wirth, M., and Wendisch, M.: A comprehensive in-situ and remote sensing data set collected during the HALO–(AC)[3] aircraft campaign, Earth System Science Data Discussions, 2024, 1–49, https://doi.org/10.5194/essd-2024-281, 2024.

Erfani, E. and Mitchell, D. L.: Growth of ice particle mass and projected area during riming, Atmospheric Chemistry and Physics, 17, 1241–1257, https://doi.org/10.5194/acp-17-1241-2017, 2017.

Fairall, C. W., Bradley, E. F., Hare, J. E., Grachev, A. A., and Edson, J. B.: Bulk Parameterization of Air–Sea Fluxes: Updates and Verification for the COARE Algorithm, Journal of Climate, 16, 571–591, https://doi.org/10.1175/1520-0442(2003)016<0571:BPOASF>2.0.CO;2, publisher: American Meteorological Society Section: Journal of Climate, 2003.

Fitch, K. E. and Garrett, T. J.: Graupel Precipitating From Thin Arctic Clouds With Liquid Water Paths Less Than 50 g m^{-2}, Geophysical Research Letters, 49, https://doi.org/10.1029/2021GL094075, 2022.

Geerts, B., Giangrande, S. E., McFarquhar, G. M., Xue, L., Abel, S. J., Comstock, J. M., Crewell, S., DeMott, P. J., Ebell, K., Field, P., Hill, T. C. J., Hunzinger, A., Jensen, M. P., Johnson, K. L., Juliano, T. W., Kollias, P., Kosovic, B., Lackner, C., Luke, E., Lüpkes, C., Matthews, A. A., Neggers, R., Ovchinnikov, M., Powers, H., Shupe, M. D., Spengler, T., Swanson, B. E., Tjernström, M., Theisen, A. K., Wales, N. A., Wang, Y., Wendisch, M., and Wu, P.: The COMBLE Campaign: A Study of Marine Boundary Layer Clouds in Arctic Cold-Air Outbreaks, Bulletin of the American Meteorological Society, 103, E1371–E1389, https://doi.org/10.1175/BAMS-D-21-0044.1, 2022.

George, G., Stevens, B., Bony, S., Pincus, R., Fairall, C., Schulz, H., Kölling, T., Kalen, Q. T., Klingebiel, M., Konow, H., Lundry, A., Prange, M., and Radtke, J.: JOANNE: Joint dropsonde Observations of the Atmosphere in tropical North atlaNtic meso-scale Environments, Earth Syst. Sci. Data, 13, 5253–5272, https://doi.org/10.5194/essd-13-5253-2021, 2021.

Gryschka, M., Drüe, C., Etling, D., and Raasch, S.: On the influence of sea-ice inhomogeneities onto roll convection in cold-air outbreaks, Geophysical Research Letters, 35, https://doi.org/10.1029/2008GL035845, 2008.

Gryschka, M., Fricke, J., and Raasch, S.: On the impact of forced roll convection on vertical turbulent transport in cold air outbreaks, Journal of Geophysical Research: Atmospheres, 119, 12–513, 2014.

Hein, P. F. and Brown, R. A.: Observations of longitudinal roll vortices during arctic cold air outbreaks over open water, Boundary-Layer Meteorology, 45, 177–199, https://doi.org/10.1007/BF00120822, 1988.

Hersbach, H., Bell, B., Berrisford, P., Hirahara, S., Horányi, A., Muñoz-Sabater, J., Nicolas, J., Peubey, C., Radu, R., Schepers, D., Simmons, A., Soci, C., Abdalla, S., Abellan, X., Balsamo, G., Bechtold, P., Biavati, G., Bidlot, J., Bonavita, M., De Chiara, G., Dahlgren, P., Dee, D., Diamantakis, M., Dragani, R., Flemming, J., Forbes, R., Fuentes, M., Geer, A., Haimberger, L., Healy, S., Hogan, R. J., Hólm, E., Janisková, M., Keeley, S., Laloyaux, P., Lopez, P., Lupu, C., Radnoti, G., de Rosnay, P., Rozum, I., Vamborg, F., Villaume, S., and Thépaut, J.-N.: Complete ERA5 from 1940: Fifth generation of ECMWF atmospheric reanalyses of the global climate, Copernicus Climate Change Service (C3S) Data Store (CDS), https://doi.org/10.24381/cds.143582cf, (last access: 03 November 2023) [data], 2017.

Hersbach, H., Bell, B., Berrisford, P., Hirahara, S., Horányi, A., Muñoz-Sabater, J., Nicolas, J., Peubey, C., Radu, R., Schepers, D., Simmons, A., Soci, C., Abdalla, S., Abellan, X., Balsamo, G., Bechtold, P., Biavati, G., Bidlot, J., Bonavita, M., De Chiara, G., Dahlgren, P., Dee, D., Diamantakis, M., Dragani, R., Flemming, J., Forbes, R., Fuentes, M., Geer, A., Haimberger, L., Healy, S., Hogan, R. J., Hólm, E., Janisková, M., Keeley, S., Laloyaux, P., Lopez, P., Lupu, C., Radnoti, G., de Rosnay, P., Rozum, I., Vamborg, F., Villaume, S., and Thépaut, J.-N.: The ERA5 global reanalysis, Quarterly Journal of the Royal Meteorological Society, 146, 1999–2049, https://doi.org/10.1002/qj.3803, 2020.

Hersbach, H., Bell, B., Berrisford, P., Biavati, G., Horányi, A., Muñoz Sabater, J., Nicolas, J., Peubey, C., Radu, R., Rozum, I., Schepers, D., Simmons, A., Soci, C., Dee, D., and Thépaut, J.-N.: ERA5 hourly data on pressure levels from 1940 to present, Copernicus Climate Change Service (C3S) Climate Data Store (CDS), https://doi.org/10.24381/cds.bd0915c6, (last access: 29 August 2024) [data], 2023a.

Hersbach, H., Bell, B., Berrisford, P., Biavati, G., Horányi, A., Muñoz Sabater, J., Nicolas, J., Peubey, C., Radu, R., Rozum, I., Schepers, D., Simmons, A., Soci, C., Dee, D., and Thépaut, J.-N.: ERA5 hourly data on single levels from 1940 to present, Copernicus Climate Change Service (C3S) Climate Data Store (CDS), https://doi.org/10.24381/cds.adbb2d47, (last access: 29 August 2024) [data], 2023b.

Heymsfield, A. J.: A Comparative Study of the Rates of Development of Potential Graupel and Hail Embryos in High Plains Storms, Journal of the Atmospheric Sciences, 39, 2867–2897, https://doi.org/10.1175/1520-0469(1982)039<2867:ACSOTR>2.0.CO;2, 1982.

Kirbus, B., Schirmacher, I., Klingebiel, M., Schäfer, M., Ehrlich, A., Slättberg, N., Lucke, J., Moser, M., Müller, H., and Wendisch, M.: Thermodynamic and cloud evolution in a cold air outbreak during HALO-(AC)[3]: Quasi-Lagrangian observations compared to the ERA5 and CARRA reanalyses, EGUsphere, pp. 1–40, https://doi.org/10.5194/egusphere-2023-2989, 2023.

Klingebiel, M., de Lozar, A., Molleker, S., Weigel, R., Roth, A., Schmidt, L., Meyer, J., Ehrlich, A., Neuber, R., Wendisch, M., and Borrmann, S.: Arctic low-level boundary layer clouds: in situ measurements and simulations of mono- and bimodal supercooled droplet size distributions at the top layer of liquid phase clouds, Atmospheric Chemistry and Physics, 15, 617–631, https://doi.org/10.5194/acp-15-617-2015, 2015.

Klingebiel, M., Ehrlich, A., Ruiz-Donoso, E., Risse, N., Schirmacher, I., Jäkel, E., Schäfer, M., Wolf, K., Mech, M., Moser, M., Voigt, C., and Wendisch, M.: Variability and properties of liquid-dominated clouds over the ice-free and sea-ice-covered Arctic Ocean, Atmospheric Chemistry and Physics Discussions, pp. 1–24, https://doi.org/10.5194/acp-2022-848, 2023.

Kolstad, E. W.: Higher ocean wind speeds during marine cold air outbreaks, Quarterly Journal of the Royal Meteorological Society, 143, 2084–2092, https://doi.org/10.1002/qj.3068, 2017.

Korolev, A.: Limitations of the Wegener–Bergeron–Findeisen Mechanism in the Evolution of Mixed-Phase Clouds, Journal of the Atmospheric Sciences, 64, 3372–3375, https://doi.org/10.1175/JAS4035.1, 2007.

Korolev, A. and Field, P. R.: The effect of dynamics on mixed-phase clouds: Theoretical considerations, Journal of the Atmospheric Sciences, 65, 66–86, 2008.

Korolev, A., McFarquhar, G., Field, P. R., Franklin, C., Lawson, P., Wang, Z., Williams, E., Abel, S. J., Axisa, D., Borrmann, S., Crosier, J., Fugal, J., Krämer, M., Lohmann, U., Schlenczek, O., Schnaiter, M., and Wendisch, M.: Mixed-Phase Clouds: Progress and Challenges, Meteorological Monographs, 58, 5.1 – 5.50, https://doi.org/10.1175/AMSMONOGRAPHS-D-17-0001.1, 2017.

Kuettner, J. P.: Cloud bands in the earth's atmosphere: Observations and Theory, Tellus, 23, 404–426, https://doi.org/10.3402/tellusa.v23i4-5.10519, 1971.

Kulie, M. S. and Bennartz, R.: Utilizing Spaceborne Radars to Retrieve Dry Snowfall, Journal of Applied Meteorology and Climatology, 48, 2564–2580, https://doi.org/10.1175/2009JAMC2193.1, 2009.

Lackner, C. P., Geerts, B., Juliano, T. W., Xue, L., and Kosovic, B.: Vertical structure of clouds and precipitation during Arctic cold-air outbreaks and warm-air intrusions: Observations from COMBLE, Journal of Geophysical Research: Atmospheres, 128, e2022JD038 403, 2023.

Lance, S., Brock, C. A., Rogers, D., and Gordon, J. A.: Water droplet calibration of the Cloud Droplet Probe (CDP) and in-flight performance in liquid, ice and mixed-phase clouds during ARCPAC, Atmospheric Measurement Techniques, 3, 1683–1706, https://doi.org/10.5194/amt-3-1683-2010, 2010.

Li, X., Krueger, S. K., Strong, C., Mace, G. G., and Benson, S.: Midwinter Arctic leads form and dissipate low clouds, Nature Communications, 11, 206, https://doi.org/10.1038/s41467-019-14074-5, 2020.

Ludovic, B., Byron, B., Christopher, F., Elizabeth, T., Jim, E., and Robert, P.: Python implementation of the COARE 3.5 Bulk Air- Sea Flux algorithm, https://doi.org/10.5281/zenodo.5110991, 2021.

Ludwig, V. and Spreen, G.: modis_amsr2, https://data.seaice.uni-bremen.de/modis_amsr2/, (last access: 20 October 2023) [data], 2023.

Ludwig, V., Spreen, G., and Pedersen, L. T.: Evaluation of a New Merged Sea-Ice Concentration Dataset at 1 km Resolution from Thermal Infrared and Passive Microwave Satellite Data in the Arctic, Remote Sensing, 12, 3183, https://doi.org/10.3390/rs12193183, 2020.

Maahn, M., Burgard, C., Crewell, S., Gorodetskaya, I. V., Kneifel, S., Lhermitte, S., Van Tricht, K., and van Lipzig, N. P. M.: How does the spaceborne radar blind zone affect derived surface snowfall statistics in polar regions?, Journal of Geophysical Research: Atmospheres, 119, 13,604–13,620, https://doi.org/10.1002/2014JD022079, _eprint: https://onlinelibrary.wiley.com/doi/pdf/10.1002/2014JD022079, 2014.

Mages, Z., Kollias, P., Zhu, Z., and Luke, E. P.: Surface-based observations of cold-air outbreak clouds during the COMBLE field campaign, preprint, https://doi.org/10.5194/acp-2022-546, 2022.

Maherndl, N., Maahn, M., Tridon, F., Leinonen, J., Ori, D., and Kneifel, S.: A riming-dependent parameterization of scattering by snowflakes using the self-similar Rayleigh–Gans approximation, Quarterly Journal of the Royal Meteorological Society, pp. 1–20, https://doi.org/10.1002/qj.4573, 2023a.

Maherndl, N., Moser, M., Lucke, J., Mech, M., Risse, N., Schirmacher, I., and Maahn, M.: Quantifying riming from airborne data during HALO-(AC)[3], EGUsphere, pp. 1–32, https://doi.org/10.5194/egusphere-2023-1118, 2023b.

Markson, R.: Atmospheric Electrical Detection of Organized Convection, American Association for the Advancement of Science, pp. 1171 – 1177, https://doi.org/10.1126/science.188.4194.1171, 1975.

Mateling, M. E., Pettersen, C., Kulie, M. S., and L'Ecuyer, T. S.: Marine Cold-Air Outbreak Snowfall in the North Atlantic: A CloudSat Perspective, Journal of Geophysical Research: Atmospheres, 128, https://doi.org/10.1029/2022JD038053, 2023.

McFarquhar, G. M., Zhang, G., Poellot, M. R., Kok, G. L., McCoy, R., Tooman, T., Fridlind, A., and Heymsfield, A. J.: Ice properties of single-layer stratocumulus during the Mixed-Phase Arctic Cloud Experiment: 1. Observations, Journal of Geophysical Research, 112, D24 201, https://doi.org/10.1029/2007JD008633, 2007.

Mech, M., Kliesch, L.-L., Anhäuser, A., Rose, T., Kollias, P., and Crewell, S.: Microwave Radar/radiometer for Arctic Clouds (MiRAC): first insights from the ACLOUD campaign, Atmospheric Measurement Techniques, 12, 5019–5037, https://doi.org/10.5194/amt-12-5019-2019, 2019.

Mech, M., Ehrlich, A., Herber, A., Lüpkes, C., Wendisch, M., Becker, S., Boose, Y., Chechin, D., Crewell, S., Dupuy, R., Gourbeyre, C., Hartmann, J., Jäkel, E., Jourdan, O., Kliesch, L.-L., Klingebiel, M., Kulla, B. S., Mioche, G., Moser, M., Risse, N., Ruiz-Donoso, E., Schäfer, M., Stapf, J., and Voigt, C.: MOSAiC-ACA and AFLUX - Arctic airborne campaigns characterizing the exit area of MOSAiC, Scientific Data, 9, 790, https://doi.org/10.1038/s41597-022-01900-7, 2022a.

Mech, M., Risse, N., Marrollo, G., and Paul, D.: Ac3airborne, 10.5281/zenodo.7305585, [code], 2022b.

1105 Mioche, G., Jourdan, O., Delanoë, J., Gourbeyre, C., Febvre, G., Dupuy, R., Monier, M., Szczap, F., Schwarzenboeck, A., and Gayet, J.-F.: Vertical distribution of microphysical properties of Arctic springtime low-level mixed-phase clouds over the Greenland and Norwegian seas, Atmospheric Chemistry and Physics, 17, 12 845–12 869, https://doi.org/10.5194/acp-17-12845-2017, 2017.

Morrison, H., de Boer, G., Feingold, G., Harrington, J., Shupe, M. D., and Sulia, K.: Resilience of persistent Arctic mixed-phase clouds, Nature Geoscience, 5, 11–17, https://doi.org/10.1038/ngeo1332, 2012.

1110 Moser, M., Voigt, C., Jurkat-Witschas, T., Hahn, V., Mioche, G., Jourdan, O., Dupuy, R., Gourbeyre, C., Schwarzenboeck, A., Lucke, J., Boose, Y., Mech, M., Borrmann, S., Ehrlich, A., Herber, A., Lüpkes, C., and Wendisch, M.: Microphysical and thermodynamic phase analyses of Arctic low-level clouds measured above the sea ice and the open ocean in spring and summer, preprint, https://doi.org/10.5194/acp-2023-44, 2023.

Murray-Watson, R. J., Gryspeerdt, E., and Goren, T.: Investigating the development of clouds within marine cold air outbreaks, EGUsphere,
1115 pp. 1–29, https://doi.org/10.5194/egusphere-2023-734, 2023.

Müller, G., Brümmer, B., and Alpers, W.: Roll Convection within an Arctic Cold-Air Outbreak: Interpretation of In Situ Aircraft Measurements and Spaceborne SAR Imagery by a Three-Dimensional Atmospheric Model, Monthly Weather Review, 127, 363–380, https://doi.org/10.1175/1520-0493(1999)127<0363:RCWAAC>2.0.CO;2, 1999.

Nasa Worldview: Cloud Water Path Terra / MODIS, https://go.nasa.gov/46vE70B, (last access: 21 November 2023), 2023a.

1120 Nasa Worldview: Corrected Reflectance (True Color) Terra / MODIS, https://go.nasa.gov/46o4aXO, (last access: 21 November 2023), 2023b.

Nasa Worldview: Corrected Reflectance (Bands M3-I3-M11) Suomi NPP / VIIRS, https://go.nasa.gov/47mKJjr, (last access: 21 November 2023), 2023c.

Papritz, L. and Spengler, T.: A Lagrangian Climatology of Wintertime Cold Air Outbreaks in the Irminger and Nordic Seas and Their Role in Shaping Air–Sea Heat Fluxes, Journal of Climate, 30, 2717–2737, https://doi.org/10.1175/JCLI-D-16-0605.1, 2017.

1125 Papritz, L., Pfahl, S., Sodemann, H., and Wernli, H.: A Climatology of Cold Air Outbreaks and Their Impact on Air–Sea Heat Fluxes in the High-Latitude South Pacific, Journal of Climate, 28, 342–364, https://doi.org/10.1175/JCLI-D-14-00482.1, 2015.

Pithan, F., Svensson, G., Caballero, R., Chechin, D., Cronin, T. W., Ekman, A. M. L., Neggers, R., Shupe, M. D., Solomon, A., Tjernström, M., and Wendisch, M.: Role of air-mass transformations in exchange between the Arctic and mid-latitudes, Nature Geoscience, 11, 805–812, https://doi.org/10.1038/s41561-018-0234-1, 2018.

1130 Puhakka, T. and Saarikivi, P.: Doppler radar observations of horizontal roll vortices in Finland, Helsingin yliopisto. Meteorologian laitos, University of Helsinki, Department of Meteorology, https://books.google.de/books?id=aPJKAAAACAAJ, 1986.

Ruiz-Donoso, E., Ehrlich, A., Schäfer, M., Jäkel, E., Schemann, V., Crewell, S., Mech, M., Kulla, B. S., Kliesch, L.-L., Neuber, R., and Wendisch, M.: Small-scale structure of thermodynamic phase in Arctic mixed-phase clouds observed by airborne remote sensing during a cold air outbreak and a warm air advection event, Atmospheric Chemistry and Physics, 20, 5487–5511, https://doi.org/10.5194/acp-20-
1135 5487-2020, 2020.

Schirmacher, I., Kollias, P., Lamer, K., Mech, M., Pfitzenmaier, L., Wendisch, M., and Crewell, S.: Assessing Arctic low-level clouds and precipitation from above – a radar perspective, Atmospheric Measurement Techniques, 16, 4081–4100, https://doi.org/10.5194/amt-16-4081-2023, 2023.

Seifert, A., Leinonen, J., Siewert, C., and Kneifel, S.: The Geometry of Rimed Aggregate Snowflakes: A Modeling Study, Journal of Advances in Modeling Earth Systems, 11, 712–731, https://doi.org/10.1029/2018MS001519, 2019.
1140

Shupe, M. D., Matrosov, S. Y., and Uttal, T.: Arctic Mixed-Phase Cloud Properties Derived from Surface-Based Sensors at SHEBA, Journal of the Atmospheric Sciences, 63, 697–711, https://doi.org/10.1175/JAS3659.1, 2006.

Shupe, M. D., Kollias, P., Persson, P. O. G., and McFarquhar, G. M.: Vertical Motions in Arctic Mixed-Phase Stratiform Clouds, Journal of the Atmospheric Sciences, 65, 1304–1322, https://doi.org/10.1175/2007JAS2479.1, 2008.

Spensberger, C. and Spengler, T.: Sensitivity of Air-Sea Heat Exchange in Cold-Air Outbreaks to Model Resolution and Sea-Ice Distribution, Journal of Geophysical Research: Atmospheres, 126, https://doi.org/10.1029/2020JD033610, 2021.

Sprenger, M. and Wernli, H.: The LAGRANTO Lagrangian analysis tool – version 2.0, Geoscientific Model Development, 8, 2569–2586, https://doi.org/10.5194/gmd-8-2569-2015, 2015.

Stachlewska, I. S., Neuber, R., Lampert, A., Ritter, C., and Wehrle, G.: AMALi – the Airborne Mobile Aerosol Lidar for Arctic research, Atmos. Chem. Phys., p. 17, https://doi.org/10.5194/acp-10-2947-2010, 2010.

Tornow, F., Ackerman, A. S., and Fridlind, A. M.: Preconditioning of overcast-to-broken cloud transitions by riming in marine cold air outbreaks, Atmospheric Chemistry and Physics, 21, 12 049–12 067, https://doi.org/10.5194/acp-21-12049-2021, 2021.

Tornow, F., Ackerman, A. S., Fridlind, A. M., Cairns, B., Crosbie, E. C., Kirschler, S., Moore, R. H., Painemal, D., Robinson, C. E., Seethala, C., Shook, M. A., Voigt, C., Winstead, E. L., Ziemba, L. D., Zuidema, P., and Sorooshian, A.: Dilution of Boundary Layer Cloud Condensation Nucleus Concentrations by Free Tropospheric Entrainment During Marine Cold Air Outbreaks, Geophysical Research Letters, 49, https://doi.org/10.1029/2022GL098444, 2022.

Turner, J. and Marshall, G. J.: Climate change in the polar regions, Cambridge University Press, https://books.google.de/books?id=klTlaWWWxNoC, 2011.

Vaisala: Vaisala Dropsonde RD94, https://www.vaisala.com/sites/default/files/documents/RD94-Dropsonde-Datasheet-B210936EN-A-LoRes.pdf, (last access: 31 October 2023), 2010.

Virtanen, P., Gommers, R., Oliphant, T. E., Haberland, M., Reddy, T., Cournapeau, D., Burovski, E., Peterson, P., Weckesser, W., Bright, J., van der Walt, S. J., Brett, M., Wilson, J., Millman, K. J., Mayorov, N., Nelson, A. R. J., Jones, E., Kern, R., Larson, E., Carey, C. J., Polat, İ., Feng, Y., Moore, E. W., VanderPlas, J., Laxalde, D., Perktold, J., Cimrman, R., Henriksen, I., Quintero, E. A., Harris, C. R., Archibald, A. M., Ribeiro, A. H., Pedregosa, F., van Mulbregt, P., and SciPy 1.0 Contributors: SciPy 1.0: Fundamental Algorithms for Scientific Computing in Python, Nature Methods, 17, 261–272, https://doi.org/10.1038/s41592-019-0686-2, 2020.

von Lerber, A., Mech, M., Rinke, A., Zhang, D., Lauer, M., Radovan, A., Gorodetskaya, I., and Crewell, S.: Evaluating seasonal and regional distribution of snowfall in regional climate model simulations in the Arctic, Atmospheric Chemistry and Physics, 22, 7287–7317, https://doi.org/10.5194/acp-22-7287-2022, 2022.

Walbröl, A., Michaelis, J., Becker, S., Dorff, H., Ebell, K., Gorodetskaya, I., Heinold, B., Kirbus, B., Lauer, M., Maherndl, N., Maturilli, M., Mayer, J., Müller, H., Neggers, R. A. J., Paulus, F. M., Röttenbacher, J., Rückert, J. E., Schirmacher, I., Slättberg, N., Ehrlich, A., Wendisch, M., and Crewell, S.: Contrasting extremely warm and long-lasting cold air anomalies in the North Atlantic sector of the Arctic during the HALO-$(\mathcal{AC})^3$ campaign, Atmospheric Chemistry and Physics, 24, 8007–8029, https://doi.org/10.5194/acp-24-8007-2024, 2024.

Walter, B. A. and Overland, J. E.: Observations of Longitudinal Rolls in a Near Neutral Atmosphere, Monthly Weather Review, 112, 200–208, https://doi.org/10.1175/1520-0493(1984)112<0200:OOLRIA>2.0.CO;2, 1984.

Wendisch, M., Handorf, D., Tegen, I., Neggers, R., and Spreen, G.: Glimpsing the Ins and Outs of the Arctic Atmospheric Cauldron, Eos, 102, https://doi.org/https://doi.org/10.1029/2021EO155959, 2021.

Wendisch, M., Brückner, M., Crewell, S., Ehrlich, A., Notholt, J., Lüpkes, C., Macke, A., Burrows, J. P., Rinke, A., Quaas, J., Maturilli, M., Schemann, V., Shupe, M. D., Akansu, E. F., Barrientos-Velasco, C., Bärfuss, K., Blechschmidt, A.-M., Block, K., Bougoudis, I.,

Bozem, H., Böckmann, C., Bracher, A., Bresson, H., Bretschneider, L., Buschmann, M., Chechin, D. G., Chylik, J., Dahlke, S., Deneke, H., Dethloff, K., Donth, T., Dorn, W., Dupuy, R., Ebell, K., Egerer, U., Engelmann, R., Eppers, O., Gerdes, R., Gierens, R., Gorodetskaya, I. V., Gottschalk, M., Griesche, H., Gryanik, V. M., Handorf, D., Harm-Altstädter, B., Hartmann, J., Hartmann, M., Heinold, B., Herber, A., Herrmann, H., Heygster, G., Höschel, I., Hofmann, Z., Hölemann, J., Hünerbein, A., Jafariserajehlou, S., Jäkel, E., Jacobi, C., Janout, M., Jansen, F., Jourdan, O., Jurányi, Z., Kalesse-Los, H., Kanzow, T., Käthner, R., Kliesch, L. L., Klingebiel, M., Knudsen, E. M., Kovács, T., Körtke, W., Krampe, D., Kretzschmar, J., Kreyling, D., Kulla, B., Kunkel, D., Lampert, A., Lauer, M., Lelli, L., Lerber, A. v., Linke, O., Löhnert, U., Lonardi, M., Losa, S. N., Losch, M., Maahn, M., Mech, M., Mei, L., Mertes, S., Metzner, E., Mewes, D., Michaelis, J., Mioche, G., Moser, M., Nakoudi, K., Neggers, R., Neuber, R., Nomokonova, T., Oelker, J., Papakonstantinou-Presvelou, I., Pätzold, F., Pefanis, V., Pohl, C., Pinxteren, M. v., Radovan, A., Rhein, M., Rex, M., Richter, A., Risse, N., Ritter, C., Rostosky, P., Rozanov, V. V., Donoso, E. R., Garfias, P. S., Salzmann, M., Schacht, J., Schäfer, M., Schneider, J., Schnierstein, N., Seifert, P., Seo, S., Siebert, H., Soppa, M. A., Spreen, G., Stachlewska, I. S., Stapf, J., Stratmann, F., Tegen, I., Viceto, C., Voigt, C., Vountas, M., Walbröl, A., Walter, M., Wehner, B., Wex, H., Willmes, S., Zanatta, M., and Zeppenfeld, S.: Atmospheric and Surface Processes, and Feedback Mechanisms Determining Arctic Amplification: A Review of First Results and Prospects of the (AC)3 Project, Bulletin of the American Meteorological Society, 104, E208–E242, https://doi.org/10.1175/BAMS-D-21-0218.1, 2023.

Wendisch, M., Crewell, S., Ehrlich, A., Herber, A., Kirbus, B., Lüpkes, C., Mech, M., Abel, S. J., Akansu, E. F., Ament, F., Aubry, C., Becker, S., Borrmann, S., Bozem, H., Brückner, M., Clemen, H.-C., Dahlke, S., Dekoutsidis, G., Delanoë, J., De La Torre Castro, E., Dorff, H., Dupuy, R., Eppers, O., Ewald, F., George, G., Gorodetskaya, I. V., Grawe, S., Groß, S., Hartmann, J., Henning, S., Hirsch, L., Jäkel, E., Joppe, P., Jourdan, O., Jurányi, Z., Karalis, M., Kellermann, M., Klingebiel, M., Lonardi, M., Lucke, J., Luebke, A., Maahn, M., Maherndl, N., Maturilli, M., Mayer, B., Mayer, J., Mertes, S., Michaelis, J., Michalkov, M., Mioche, G., Moser, M., Müller, H., Neggers, R., Ori, D., Paul, D., Paulus, F., Pilz, C., Pithan, F., Pöhlker, M., Pörtge, V., Ringel, M., Risse, N., Roberts, G. C., Rosenburg, S., Röttenbacher, J., Rückert, J., Schäfer, M., Schäfer, J., Schemannn, V., Schirmacher, I., Schmidt, J., Schmidt, S., Schneider, J., Schnitt, S., Schwarz, A., Siebert, H., Sodemann, H., Sperzel, T., Spreen, G., Stevens, B., Stratmann, F., Svensson, G., Tatzelt, C., Tuch, T., Vihma, T., Voigt, C., Volkmer, L., Walbröl, A., Weber, A., Wehner, B., Wetzel, B., Wirth, M., and Zinner, T.: Overview: Quasi-Lagrangian observations of Arctic air mass transformations – Introduction and initial results of the HALO–(AC)[3] aircraft campaign, EGUsphere, 2024, 1–46, https://doi.org/10.5194/egusphere-2024-783, 2024.

Wesche, C., Steinhage, D., and Nixdorf, U.: Polar aircraft Polar5 and Polar6 operated by the Alfred Wegener Institute, Journal of large-scale research facilities JLSRF, 2, A87–A87, https://doi.org/10.17815/jlsrf-2-153, 2016.

Ziereis, H. and Gläßer, M.: HALO - Global Player für die Atmosphärenforschung, DLR Nachrichten, pp. 32–36, 2006.